Clear-column radiative closure during ACE-Asia: Comparison of multiwavelength extinction derived from particle size and composition with results from sunphotometry

J. Wang[1], R. C. Flagan[1], J. H. Seinfeld[1], H. H. Jonsson[2], D. R. Collins[3], P. B. Russell[4], B. Schmid[5], J. Redemann[5], J. M. Livingston[6], S. Gao[7], D. A. Hegg[7], E. J. Welton[8], and D. Bates[9]

Short title: RADIATIVE CLOSURE

---

[1]Department of Chemical Engineering, California Institute of Technology, Pasadena, California

[2]Department of Meteorology, Naval Postgraduate School, Monterey, California

[3]Department of Atmospheric Sciences, Texas A&M University, College Station, Texas

[4]NASA Ames Research Center, Moffett Field, California

[5]Bay Area Enviornmental Research Institute, Sonoma, California

[6]SRI international, Menlo Park, California

[7]Department of Atmospheric Sciences, University of Washington, Seattle, Washington

[8]NASA Goddard Earth Sciences and Technology Center and University of Maryland Baltimore County, Greenbelt, Maryland

[9]Physics Department, University of Miami, Coral Gables, Florida

Abstract. From March to May 2001, aerosol size distributions and chemical compositions were measured using differential mobility analyzers, an aerodynamic particle sizer, Micro-Orifice Uniform Deposit Impactors, and denuder samplers onboard the Twin Otter aircraft as part of the ACE-Asia campaign. Of the 19 research flights, measurements on 4 flights that represented different aerosol characteristics are analyzed in detail. Clear-column radiative closure is studied by comparing aerosol extinctions predicted using in situ aerosol size distribution and chemical composition measurements to those derived from the 14-wavelength NASA Ames Airborne Tracking Sunphotometer (AATS-14). In the boundary layer, pollution layers, and free troposphere with no significant mineral dust present, aerosol extinction closure was achieved within the estimated uncertainties over the full range of wavelengths of AATS-14. Aerosol extinctions predicted based on measured size distributions also reproduce the wavelength dependence derived from AATS-14 data. Considering all four flights, the best-fit lines yield Predicted/Observed ratios in boundary and pollution layers of 0.96 and 1.03 at $\lambda = 525$ nm, and 0.94 and 1.04 at $\lambda = 1059$ nm, respectively. In free troposphere dust layers, aerosol extinctions predicted from the measured size distributions were generally smaller than those derived from the AATS-14 data; the Predicted/Observed ratios are 0.65 and 0.66 at 525 nm and 1059 nm, respectively. A detailed analysis suggests that the discrepancy is likely a result of the lack of the knowledge of mineral dust shape, as well as variations in aerosol extinction derived from AATS-14 data when viewing through horizontally inhomogeneous layers.

1. Introduction

Quantifying the effect of atmospheric aerosols on the climate system requires knowledge of their physical, chemical, and optical properties, as well as of their temporal and spatial variability. ACE-Asia was designed to study the aerosol in the atmosphere of East Asia, one of the Earth's most significant and complex anthropogenic aerosol sources. With widespread fossil fuel and biomass burning, coupled with large outbreaks of mineral dust, the atmospheric aerosol leaving the Asian continent is, arguably, the most complex on Earth. Through simultaneous measurement of aerosol microphysical, chemical, and radiative properties from a variety of platforms, the ACE-Asia campaign provided data to assess the climate impact of Asian aerosol.

A fundamental question that underlies prediction of aerosol climatic effects is how accurately aerosol radiative properties can be predicted based on measured in situ microphysical and chemical properties. If it can be demonstrated that columnar aerosol extinction and other radiative properties (e.g., absorption, angular distribution of scattering) can be accurately predicted given the knowledge of atmospheric aerosol size and composition, then models that predict these properties can be confidently used to predict climatic effects of aerosols. This so-called radiative closure has been attempted with varying degrees of success in several field campaigns using a variety of over-determined measurements and modelling techniques [*Clarke et al.*, 1996; *Hoff et al.*, 1996; *Hegg et al.*, 1997; *Howell and Huebert*, 1998; *Redemann et al.*, 1998; *Collins et*

al., 2000]. ACE-Asia was planned to provide an unprecedented opportunity to perform aerosol radiative closure studies from a number of platforms. This paper focuses on radiative closure between the aerosol extinction calculated using in situ measurements of aerosol size distributions and chemical compositions aboard the CIRPAS Twin Otter aircraft and those derived from the 14-wavelength NASA Ames Airborne Tracking Sunphotometer (AATS-14), which flew on the same aircraft.

ACE-Asia was conducted in East Asia from late March to early May, 2001. Intensive field measurements were conducted off the coast of east China, Korea, and Japan. A detailed description of the campaign is given by *Huebert et al.* [2002] (Overview paper). The CIRPAS Twin Otter flew 19 scientific missions out of Iwakuni Marine Corps Air Station, Japan. Four of those missions sampling different air masses provided ideal conditions for detailed analysis of predicted and observed clear column aerosol extinction, and we address these four cases in detail in the present paper.

2. Aerosol Size Distribution Measurements

The suite of instruments related to this study, which are deployed on the Twin Otter, are listed in Table 1. Measurements and data reduction for each instrument are described in detail in this section. Because it is essential to assess the uncertainty associated with the eventual radiative closure, and because some of that uncertainty results from uncertainties in the aerosol size and composition measurements, we devote attention to a careful analysis of the measurements on which the radiative closure is based.

Table 1.

2.1. Differential Mobility Analyzer (DMA)

Two differential mobility analyzer (DMA) systems, operated in parallel inside the main cabin of the Twin Otter, were deployed during ACE-Asia [*Wang et al.*, 2002]. One of the two systems measures the dry aerosol size distribution by passing the aerosol flow through a Nafion drier prior to the measurement. The other measures the aerosol size distribution at ambient relative humidity (RH) by using an active RH controller, which maintains the RH of the aerosol flow at ambient level by actively adding or removing water vapor from the flow [*Wang et al.*, 2002]. The size measurement sections of the two systems downstream of the drier and active RH controller are identical. The main components of the measurement section are a cylindrical DMA (TSI Inc., model 3081) and a condensation particle counter (TSI Inc., model 3010), which has a 50% counting efficiency at 10 nm. All the flows associated with the DMA are monitored and maintained by feedback controllers to compensate for environmental changes during airborne measurement. Using the scanning mobility technique, each DMA system generates a size distribution from 15 nm to 1 μm diameter every 100 s. Both DMA systems were carefully calibrated prior to and during ACE-Asia, and accurately recovered both the peak size and number concentration of monodisperse calibration aerosols as small as 30 nm diameter. The aerosol sample flows for the DMA systems were drawn from the Twin Otter community inlet, which was shared by other instruments in the main cabin. For the particle size range measured by the DMA systems (diameters smaller than 1 μm), the aerosol transmission efficiency through the community inlet has

been established to be 100%. Data from DMA systems were analyzed using the data inversion procedure described by *Collins et al.* [2002a].

2.2. Aerodynamic Particle Sizer (APS)

An aerodynamic particle sizer (APS, TSI model 3320), which has a measurement range of 0.5 μm to 20 μm in aerodynamic diameter, was mounted under the left wing of the Twin Otter. The APS infers particle size by measuring the velocity of particles inertially accelerated in an expanding air stream; large particles undergo smaller acceleration and achieve lower velocity than small particles. Note that the APS does not measure the traditional aerodynamic particle size, for reasons that are explained below.

Independent of the sampling pressure, i.e. aircraft altitude, the velocity of expanding air downstream of the APS nozzle reaches 150 m/s. The particle Reynolds number inside the acceleration region is defined as

$$\mathrm{Re_p} = \frac{\rho_\mathrm{g} D_\mathrm{p} (V_\mathrm{g} - V_\mathrm{p})}{\eta} \tag{1}$$

where ρ_g is the density of air, $D_\mathrm{p} = \sqrt[3]{\frac{6V}{\pi}}$ is the particle volume-equivalent diameter, where V is the volume of the particle. V_g is the air speed in the instrument, V_p the speed of the accelerated particle, and η the viscosity of air. For polystyrene latex (PSL) particles with diameters of 1.0, 2.1, 5, and 15 μm, the corresponding values of $\mathrm{Re_p}$ in the acceleration region are 0.65, 4.8, 24, and 103, respectively [*Wang and John*, 1987]. Therefore, the interaction of the particle and the surrounding air often lies well outside the Stokes regime ($\mathrm{Re_p} < 0.05$). Under the ultra-Stokesian condition ($\mathrm{Re_p} > 0.05$), the

particle speed after acceleration is a function of particle aerodynamic size as well as the density of the particle [*Wilson and Liu*, 1980; *Baron*, 1984)]. In an attempt to quantify the effect of particle density on APS measurement, *Wang and John* [1987] found that within the resolution of the instrument, inside the detection volume, two particles with the same velocity, i.e. the same APS response, have the same acceleration. This finding enables accurate interpretation of APS measurements provided with calibration data. *Cheng et al.* [1990] generalized the analysis to include particle shape and slip correction factor. For two particles with the same APS response, the following relationship holds:

$$\left.\frac{\kappa(1+a_2\mathrm{Re}_{\mathrm{p2}}^{b_2})}{\rho_{\mathrm{p2}}D_{\mathrm{p2}}^2C(D_{\mathrm{p2}})}\right|_2 = \left.\frac{(1+a_1\mathrm{Re}_{\mathrm{p1}}^{b_1})}{\rho_{\mathrm{p1}}D_{\mathrm{p1}}^2C(D_{\mathrm{p1}})}\right|_1 \tag{2}$$

where subscript 1 denotes the calibration particle (In the present case, spherical PSL particles, density = 1.05 g/cm^3), and subscript 2 denotes the particle of interest. ρ_{p} is the particle density, C the slip correction factor, κ the dynamic shape factor, and $(1+a\mathrm{Re}^b)$ the ultra-Stokesian correction factor. For a spherical calibration particle, $\kappa = 1$, $a = 1/6$, and $b = 2/3$. The slip correction factor and the Reynolds number are evaluated at the APS sensing volume, which has a lower pressure and temperature than the ambient condition as a result of the expansion of the air stream. Given the calibration particle diameter, d_{v1}, and its density, ρ_{p1}, the volume-equivalent diameter of the measured particle, d_{v2}, can be derived using Eqn. (2) with knowledge of its density, ρ_{p2}, the dynamic shape factor, κ, and the ultra-Stokesian correction $(1+a_2\mathrm{Re}_{\mathrm{p2}}^{b_2})$.

The density of the measured particle is calculated using the size-resolved particle

chemical composition, together with its water content, which is calculated using the gas-aerosol thermodynamic model, ISORROPIA [*Nenes et al.*, 1998]. The details of the density calculation are described subsequently. In this study, particles are assumed to be spherical, a reasonable assumption for hygroscopic aerosols in the marine boundary layer, where most often the aerosols are deliquesced as a result of high relative humidity. For particles at low RH and non-hygroscopic particles, such as mineral dust, the assumption of sphericity does not necessarily hold. Lack of knowledge of dust particle shape as well as its dynamic shape factor κ, and the ultra-Stokesian correction factor $(1 + a_2 \mathrm{Re}_2^{b_2})$, is a source of uncertainty in APS measurements. Uncertainties in the aerosol extinction calculation resulting from the assumption of spherical particles is estimated by using data on nonspherical agglomerate particles measured by *Cheng et al.* [1993].

The APS occasionally detects recirculating particles within the detection region, leading to so-called artificial particles. The particles involved are generally small in size but, due to recirculation, cross the detection laser beams multiple times with a reduced speed. As a result, when this occurs, these small, but slow particles are misinterpreted as large particles. While on a number concentration basis, these artificial particles represent only a very small fraction of the total particles detected, because these particles are interpreted as large (> 5 μm), this could introduce significant errors into an aerosol extinction calculation. These artificial particles can be removed by applying a matrix data mask to the correlated APS data, which is a simultaneous measurement of the particle speed and scattering intensity as they cross the laser beams. Based on the

principle that large particles scatter more light than small particles, a particle sized to be large (slow speed) but associated with little light-scattering is identified as artificial and removed from the data. Figure 1 shows an example of the correlated data, which were taken during Research Flight 9 on April 14, 2001. The x-axis is the light scattering channel, which increases in the direction of increasing intensity of light scattered by particle. The y-axis is the time of flight channel, which increases with increasing particle time of flight between the two detection laser beams, i.e. aerodynamic particle size. The data mask is represented by a straight line in the two-dimensional time of flight-scattering intensity space. Particles appearing below the line are identified as artificial and removed. The mask given by the dashed line (TSI carbon mask) is based on the calculation of light scattered by black carbon particles; the solid line is a custom mask constructed based on ACE-Asia data. Analysis of data using each of the two data masks is considered in the case studies.

Figure 1.

APS measurements of liquid droplets are also susceptible to errors due to droplet deformation, especially near the upper size limit of the APS. *Griffiths et al.* [1986] found for 15 μm droplets that the sizes measured by the APS are 7%-20% smaller than the true size depending on the liquid used to generate the droplet. Droplet deformation is characterized by the Weber number, which is the ratio of aerodynamic drag force to the surface tension of droplet. For water droplets, the Weber number within the APS size range is less than half of the critical value, the point at which the deformation become significant. In addition, for APS measurements during ACE-Asia, large droplets, which are often dominated by NaCl (sea salt), have a smaller Weber number than that of pure

water droplets as a result of increased surface tension. Thus, droplet deformation can be neglected as a source of error in ACE-Asia APS data.

The commercial APS has been engineered for laboratory measurement. A special inlet for airborne sampling was developed by MSP Corp. to minimize impaction particle losses when transporting particles in a high speed air stream to the instrument (Figure 2). The flow rate of the APS inlet system, 100 L/min, is equal to the product of the average aircraft cruising speed, i.e. 50 m/s, and the cross-sectional area of the inlet diffuser tip. The actual instantaneous flow rate may be somewhat different from the average value, 100 L/min, and the resulting uncertainty in predicted aerosol extinction is discussed subsequently. After entering the inlet diffuser, the flow slows down significantly. The ID of the inlet diffuser tip is 0.66 cm and the ID at the end of the 7 degree diffuser is 2.54 cm. The flow then enters a virtual impactor, where it is split in a 25/75 ratio. The flow division is achieved by a flow splitter with two carefully sized orifices, the performance of which was confirmed experimentally under typical flight conditions. A small fraction (5 L/min) of the major flow after the division (75 L/min) is sampled by the APS, and the remainder of the flow (70 L/min) is removed from the system with the minor flow.

Figure 2.

The total counting efficiency of the APS measurement, η_{t}, is

$$\eta_{\mathrm{t}} = \eta_{\mathrm{s}}\eta_{\mathrm{APS}}, \tag{3}$$

where η_{s} is the transmission efficiency of the airborne inlet system and η_{APS} is the

counting efficiency of the APS. η_s is determined using uranine-tagged oleic acid particles, which are generated by a TSI vibrating orifice aerosol generator. The efficiency was calculated from the mass of aerosol collected on the 5 L/min APS tube with respect to the total mass entering the sampling system at 100 L/min flow rate, multiplied by the flow split ratio (i.e. 20).

The counting efficiency of the APS is a product of aspiration (η_{asp}), transmission (η_{tran}), and detection (η_{det})efficiencies:

$$\eta_{\text{APS}} = \eta_{\text{asp}}\eta_{\text{tran}}\eta_{\text{det}} \tag{4}$$

The aspiration and transmission efficiencies characterize the super-isokinetic sampling of the APS inner inlet and the particle deposition on the inner nozzle, respectively. The detection efficiency is defined as the fraction of particles entering the detection area that are counted.

Figure 3.

While APS counting efficiency APS has received a lot of attention, the only study of the counting efficiency of the most recent model 3320, that deployed on the Twin Otter, is apparently that of *Armendariz and Leith* [2002]. The counting efficiency from *Armendariz and Leith* [2002] and that of an earlier model (3310) from *Kinney and Pui* [1995] are shown in Figure 3. Due to the problem of artificial particles appearing in the large size range, *Armendariz and Leith* [2002] reported the counting efficiency of particles only smaller than 5 μm. The data show that the counting efficiency of the APS 3320 begins at 30% for 0.5 μm diameter particles, increases to 100% for 0.9 μm particles, then drops to 60% for 5 μm particles. The non-unity counting efficiency around 0.5 μm

is probably due to the low detection efficiency, a result of low scattering light intensity of submicron particles. In this study, APS measurements below 0.7 μm were not used, since the detection efficiency varies for particles with different refractive indices.

Kinney and Pui [1995] studied the product of the aspiration and transmission efficiencies ($\eta_{\text{asp}}\eta_{\text{tran}}$) of the earlier 3310 model. Since the APS 3320 has a similar design of the inlet geometry and similar flow characteristics to those of the 3310 model, the detection efficiency of the APS 3320 within the overlap region of the two measurements can be approximated by the ratio of reported efficiencies (Figure 3). Assuming the detection efficiency is constant for particles larger than 2 μm, the counting efficiency of the APS 3320 can be extrapolated from Kinney and Pui's results to diameters exceeding 5 μm. The assumption of a constant detection efficiency is supported by the detection efficiency derived in the overlap region, which shows little variation. To account for the potential error in the extrapolation of the APS counting efficiency, a $\pm$50% uncertainty is assumed for the APS concentration over the extrapolation size range in the uncertainty analysis of the aerosol extinction calculation.

2.3. Integration of size measurements

Adjusting the DMA and APS measurements to ambient size distributions, which are needed for extinction calculations, requires knowledge of measurement conditions inside each instrument as well as the response of aerosol size to the RH change. For the DMA system with active RH control, the RH inside the instrument was generally maintained at the ambient level and little correction was needed. However, when the

aircraft sampled airmasses with rapid RH variation, the RH inside the instrument lagged somewhat behind the ambient RH. The RH inside the DMA was continuously monitored and recorded. Determining deviation of the APS measurement RH from the ambient RH inside the APS is more complicated than for the DMAs since neither RH nor temperature of the sample flow is directly measured. Assuming no heat exchange between the aerosol flow and the conduit wall, the temperature of the air stream increases about 1.2°C as the flow decelerates in the diffuser. The residence time of the air flow before reaching the APS is about 0.4 s, which is sufficient for particles up to 20 μm diameter to adjust to the decreased RH. Before reaching the sensing volume, the RH of the aerosol flow once again changes as a result of acceleration through the APS nozzle. However, the resulting lower temperature and higher RH will not further change the particle size, since the time between acceleration and detection is about 1 μs. Since the water vapor concentration is conserved during transport of the air stream to the APS, the RH of the APS measurement was calculated from the ambient RH assuming a 1.2°C increase in temperature. The sensitivity of calculated aerosol extinction to the amount of APS ram-heating is discussed later.

2.4. Aerosol chemical composition and mixing state

Back-calculation of the *ambient* particle size distribution from each instrument's data requires knowledge of the size response to RH. Interpretation of APS data requires the particle density, which, in turn, generally necessitates knowledge of aerosol chemical composition and mixing state. The construction of aerosol chemical composition is

discussed in this section, and the two sections following focus on the calculation of the aerosol size response to RH and aerosol density. On board the Twin Otter, a set of 8 Micro-Orifice Uniform Deposit Impactors (MOUDI) and three denuder samplers were deployed to characterize aerosol chemical compositions. The sample flow rate of the MOUDI is 100 L/min. Each MOUDI has 5 stages that collect particles within predetermined aerodynamic diameter ranges. However, only one stage of each MOUDI was used to collect particles (below 3 μm) during the ACE-Asia campaign. The 8 MOUDIs enable sampling of multiple representative air mass during each flight. The MOUDI sample filters were extracted using deionized water (HPLC grade) through mechanical shaking for 20 minutes. The filter extracts were then analyzed for the metallic elements using an inductively coupled plasma - atomic emission spectrometer (ICP-AES, model Jarrell Ash 955), and water-soluble anionic species using a standard ion chromatography (IC) system (model DIONEX DX-500) [*Gao et al.*, 2002].

A pair of low-flow denuder samplers were used to collect filter samples for analysis of Organic Carbon (OC), and Elemental Carbon (EC) using a thermal-optical carbon analyzer [*Mader et al.*, 2002]. A single high-volume particle trap impactor-denuder sampler was used to collect samples for the determination of water-soluble organic carbon and individual compounds comprising the OC. Calibration experiments determined the collection efficiency of the denuder sampler is over 90% for particle with 2.3 μm diameter or smaller [*Mader et al.*, 2002].

None of the above samplers produced size-dependent information on chemical composition; thus, the following assumptions are made in order to construct the

size-resolved chemical composition. Since the concentration of NH_4^+ was not determined, the NH_4^+ concentration is estimated using the molar ratio, $NH_4^+/(2SO_4^{2-} + NO_3^-)$. Table 2 lists recent studies of aerosol chemical composition in East Asia. Ammonium to sulfate plus nitrate molar ratios among the studies range from 0.59 to 0.89. A ratio of 0.75 is assumed in this study. Based on previous observations that sulfate, nitrate, OC, and EC are found primarily in small particles, and dust and sea salt are most likely to reside in larger particles, the aerosol mass was divided into fine and coarse modes. The size boundary between the two modes will be discussed below. The fine mode consists of NH_4^+, SO_4^-, NO_3^- OC, and EC, and the coarse mode includes sea salt and dust. when the mass size distributions of the fine and coarse modes are log-normal distributions with the same geometric standard deviation, for aerosol with diameter $D_{\rm p}$, the mass ratio of the two modes could be written as

Table 2.

$$\frac{f_{\rm coarse}(D_{\rm p})}{f_{\rm fine}(D_{\rm p})} = (\frac{D_{\rm p}}{D_{\rm p0}})^{\alpha}$$
$$f_{\rm coarse}(D_{\rm p}) + f_{\rm fine}(D_{\rm p}) = 1 \qquad (5)$$

where $f_{\rm coarse}(D_{\rm p})$ and $f_{\rm fine}(D_{\rm p})$ are the mass fractions of coarse mode and fine mode in the total mass of aerosol with diameter $D_{\rm p}$, respectively. α is a positive number that ensures that the fine mode and coarse mode dominate the total mass at small and large particle sizes, respectively. It will be shown subsequently that the calculated aerosol extinction is insensitive to the value of α, and a value of 3.3 is assumed in this study. $D_{\rm p0}$ is the particle diameter at which the mass fractions of the fine mode and the coarse mode are equal to each other, 50%, which is the "size boundary" between

the two modes. D_{p0} is selected such that when Eqn. (5) is combined with the in situ aerosol size distributions, the calculated fine mode mass of aerosol matches the MOUDI and denuder sampler measurements. The mass ratios among the chemical species of the fine mode are assumed as constants, which are determined from MOUDI and denuder sampler measurements. The assumption of constant mass ratio among fine mode chemical species is supported by onboard Aerosol Mass Spectrometer size and chemically-resolved mass concentration measurements, which showed the mass ratios between $SO_4/NH_4/NO_3$/Organics were approximately independent of size in the sub-micron size range [*Bahreini et. al.*, 2002]. For the partition of sea salt and dust within the coarse mode, the majority of the coarse mode is assumed to be sea salt in the boundary and pollution layers, and dust in the free troposphere (with the exception of the April 23 case discussed later). These assumptions are necessary, since none of the samples is size-resolved, and the filters do not include all the mass above 3 μm diameter. For each flight, size-resolved chemical compositions were generated for each layer.

A Tandem DMA system was onboard the Twin Otter for measurement of aerosol hygroscopic properties [*Collins et al.*, 2002b]. The system employs two high flow DMAs to maximize the counting statistics. Hygroscopic properties of particle with diameters ranging from 40 nm to 586 nm were measured. During most of the ACE-Asia flights, the Tandem DMA data showed that aerosols of the same dry size grew to similar final size, i.e. similar water uptake when exposed to high humidity, suggesting that the particles were internally mixed. Based on these observations, the present analysis assumes internally mixed aerosols. While the mixing state of supermicron particles

is not available from hygroscopicity measurements, the assumption of an internally mixed aerosol in this size range should not cause significant errors, since frequently the supermicron aerosols were dominated by a single component, sea salt or mineral dust.

2.5. Calculation of aerosol size response to RH

Given aerosol chemical composition, the size response to varying RH was determined using the thermodynamic equilibrium model, ISORROPIA [*Nenes et al.*, 1998]. ISORROPIA describes the sodium-ammonium-chloride-sulfate-nitrate-water aerosol system, and predicts the equilibrium water content, as well as the concentration, of chemical species in both aqueous and solid phases of aerosol at given RH and temperature.

For RH between the crystallization and deliquescence points, particles can exist in either the metastable state (deliquesced) or equilibrium state (crystallized). Usually, the state of the aerosol can be determined by comparing the two size distributions measured by the DMA systems. As described above, the RH within one DMA (termed the "ambient" DMA) was maintained at ambient level by using an active RH controller. However, the size distribution measured by the "ambient" DMA is not always the true size distribution of the ambient particles. Since the RH of the aerosol flow first decreases as the flow enters the inlet, the deliquesced aerosol may be crystallized due to the initial RH decrease, and remain crystalized even after the RH later recovers to the ambient level. Therefore, we can be confident that the ambient aerosol is deliquesced only when the *aerosol measured by the "ambient" DMA* is deliquesced, which is evidenced

by a shift of the size distribution measured by the "ambient" DMA towards larger sizes as compared to the dry distribution. When particles measured by the "ambient" DMA are crystallized (identical size distributions from the two DMA systems), the true state of the ambient aerosol is less clear, especially when the ambient RH is just above the crystallization point. In this case, it is assumed that the aerosols within the boundary layer are deliquesced, and aerosols within elevated pollution layers and in the free troposphere are crystallized. Uncertainties associated with this assumption will be investigated subsequently. Organic carbon, elemental carbon, and mineral dust are considered non-hygroscopic, and are only present in the solid phase of the aerosol. This assumption is more likely to hold for elemental carbon and mineral dust, but not necessarily for many organic species likely to be present [*Saxena et al.*, 1995].

2.6. Calculation of particle density

At given RH and temperature, the aerosol density is calculated using the concentrations of both aqueous and solid phases of aerosol, which are provided by ISORROPIA. The density of the aqueous phase is calculated based on partial molar volumes,

$$\rho_a = \frac{1000 + \sum_i c_i M_i}{\frac{1000}{\rho_0} + \sum_i c_i \bar{V}_i^0 + V_{mix}^{ex}} \tag{6}$$

where ρ_a is the density of the aqueous phase, ρ_0 the density of pure water, c_i the molality of each solute, M_i the molecular weight, $\bar{V}_i^0$ the partial molar volume, and V_{mix}^{ex} the excess molal volume. In our calculation, it is assumed that no volume change associated

with mixing of water and the solutes occurs, i.e. $V_{mix}^{ex} = 0$. The error in calculated density by assuming $V_{mix}^{ex} = 0$ does not exceed 5% over the concentration range of NaCl droplets. This suggests that the assumption should not introduce significant error in the analysis since the density calculation only affects the interpretation of APS data. For the size range measured by the APS, the aqueous aerosol phase, if any, is generally dominated by NaCl.

The solid phase is assumed potentially to consist of 11 components, 8 of which are inorganic salts, and the other 3 are non-hygroscopic species: OC, EC, and mineral dust. The density of the inorganic salts are available from *CRC* [1970], and the densities of OC, EC, and mineral dust are assumed to be 1.2 [*Turpin and Lim*, 2001], 2.0 [*Fuller et al.*, 1999], and 2.5 g/cm^3[*Volz*, 1973], respectively. Once the densities of the aqueous phase and each component within the solid phase are determined, the calculation of aerosol density can be carried out.

Figure 4.

Through the calculation described above, data from the DMA and APS were used to determine the corresponding size distributions under ambient conditions. The agreement between ambient distributions derived from DMA and APS measurements usually fell within 20% in the size range within which the two instruments overlap. Figure 4 shows an example of ambient size distributions derived from DMA and APS measurements at 450 m during Research Flight 17 from UTC 1:38 to 2:09 on April 27, 2001. For the size distribution in the overlap range of the DMA and APS, a simple average of the DMA and APS distributions was used.

2.7. Effective particle refractive index

Given the chemical composition of an internally mixed particle, the optical properties are often calculated through the effective refractive index approach, assuming an equivalent homogeneous sphere with an effective, or average, refractive index, which is derived from the refractive index of each component within the aerosol. In our analysis, the refractive index of the aerosol is averaged over the aqueous phase and each component in the solid phase using the Bruggeman mixing rule [*Bruggeman*, 1935],

$$\sum_{i=1}^{n} f_{vi} \frac{m_i^2 - m_{av}^2}{m_i^2 + 2m_{av}^2} = 0 \tag{7}$$

where i indicate the aqueous phase or the different components of the solid phase within the aerosol, f_{vi} is the volume fraction, m_i the refractive index of component i, and m_{av} is the average aerosol refractive index that is being sought . With the aqueous phase composition given by ISORROPIA, the refractive index of the liquid phase can be obtained through the partial molal refraction approach [*Moelwyn-Hughes*, 1961]. The refractive indices of the 8 inorganic salts of the solid phase are taken from *CRC* [1970], and OC and EC are assumed to have refractive indies of $1.55 + 0i$ [*Larson et al.*, 1988] and $1.99 + 0.66i$ [*Seinfeld and Pandis*, 1998], respectively. With no available data on the refractive index of East Asia mineral dust, the refractive index of central Asia dust [*Sokolik et al.*, 1993], $1.5 + 0.003i$, was used. The refractive index of each component is assumed constant within the AATS-14 wavelength range (363 nm - 1558 nm). Both experimental [*Chýlek et al.*, 1988] and modelling studies [*Videen and Chýlek*,

1998] demonstrate that the Bruggeman mixing rule predicts aerosol extinction well for composite particles. The aerosol extinction was also calculated using volume-averaged refractive indices to estimate the uncertainties introduced by the average method.

2.8. Optical measurements and calculation

The 14-wavelength NASA Ames Airborne Tracking Sunphotometer (AATS-14) was deployed on the Twin Otter. The AATS-14 continuously measured the optical depth of the column of air between the aircraft and the top of atmosphere. By subtracting from this value the optical depth due to Rayleigh scattering of gas molecules and absorption by O_3, NO_2, H_2O, and O_2-O_2 (see *Schmid et al.*, 2002), the aerosol optical depth (AOD) throughout the column of air between the altitude of the aircraft and the top of the atmosphere is calculated. The derivative of AOD with respect to altitude gives the aerosol extinction σ_{ext} at different altitudes,

$$\sigma_{ext}(z,\lambda) = \frac{d\tau(z,\lambda)}{dz}, \tag{8}$$

where $\tau(z,\lambda)$ is the aerosol optical depth (AOD) at wavelength λ, and z is the distance between the instrument and top of atmosphere. Prior to differentiation, $\tau(z,\lambda)$ is smoothed (in a non-biased manner) to reduce effects of horizontal and temporal variations of AOD on the photometer-to-sun path at a given altitude (see, e.g., *Schmid et al.*, 2000). Uncertainties in derived aerosol extinction introduced by the smoothing procedure are estimated as 0.005 km^{-1} [*Schmid et al.*, 2000].

To compare with extinction derived from the AATS-14 data, aerosol extinction

is calculated using ambient aerosol size distributions together with effective refractive indices based on aerosol chemical compositions. For each particle diameter, the extinction cross-section is calculated using Mie theory at the 13 wavelengths measured by the sunphotometer (One of the 14 wavelengths was used for the measurement of water vapor concentration). The aerosol extinction is an integration over the measured size range,

$$\sigma_{\rm ext}(z,\lambda) = \int_{D_{\rm p1}}^{D_{\rm p2}} \frac{\pi}{4} D_{\rm p}^2 Q_{\rm ext}(D_{\rm p},\lambda,m(D_{\rm p},{\rm RH},z)) n(D_{\rm p},z) dlog D_{\rm p} \qquad (9)$$

where $D_{\rm p}$ is the particle diameter over which the integral is performed. $D_{\rm p1}$ and $D_{\rm p2}$ are the minimum and maximum diameters of measurement, respectively. $Q_{\rm ext}$ is the extinction cross section based on Mie theory, $m(D_{\rm p},{\rm RH},z)$ the effective refractive index of the particle, which is a function of the particle's size, composition, and (implicitly) ambient relative humidity. $n(D_{\rm p},z)$ is the particle size distribution at ambient conditions.

2.9. Uncertainty analysis

Table 3.

The degree to which clear column radiative closure is achieved is judged by the closeness with which measured and calculated extinctions agree. To understand discrepancies between the calculated and measured $\sigma_{\rm ext}$, the uncertainties associated with the calculated aerosol extinction need to be addressed. The uncertainty sources, which are grouped into 7 categories, are listed in Table 3, together with the uncertainty levels assumed in the analysis. Many of the entries in Table 3 have been discussed

above. To examine the uncertainty associated with aerosol mixing state, we carried out a complete calculation based on an externally mixed aerosol, in which 8 types of aerosol were assumed: $(NH_4)_2SO_4$, NH_4HSO_4, H_2SO_4, NH_4NO_3, OC, EC, sea salt, and dust. For this externally mixed aerosol, the water content of hygroscopic aerosol and its density were calculated using data of *Tang and Munkelwitz* [1994], *Tang* [1996], and *Tang et al.* [1997]. The aerosol extinction is the summation of the contribution from each type of aerosol. The organic molecular weight per carbon weight, $m_{\rm oc}/m_{\rm c}$, value of 2.1 ± 0.2 was used in our study [*Turpin and Lim*, 2001]. $m_{\rm ions}/m_{\rm carbon}$ is the mass ratio of fine mode ions (NH_4^+, SO_4^{2-}, and NO_3^-) from the MOUDI sample to total carbon from the denuder filter samples. The $\pm 30\%$ uncertainty assumed for this ratio accounts for the different cut sizes and uncertainties in the analysis of the MOUDI and denuder filter samples. The results of the uncertainty analysis are presented with each of the four cases studied.

3. Radiative Closure

During ACE-Asia, 19 Twin Otter research flights were conducted out of Iwakuni Japan [*Huebert et al.*, 2002]. Among those 19 missions, four flights sampling different air masses presented conditions ideal for detailed analysis of clear-column radiative closure.

Figure 5.

3.1. Research Flight 14, April 23, 2001

During Research Flight 14, the Twin Otter flew to 33°N and 134°E, southeast of Shikoku Island; the flight track is shown in the top two panels of Figure 5. Three layers were sampled in detail. Two layers were within the marine boundary layer (MBL), and centered at 30 m and 600 m. The third layer was within the free troposphere and centered at an altitude of 1900 m.

The total particle number concentration showed little variation within each layer, except for occasional spikes, which may represent small regions in which recent nucleation events occurred. The total particle number concentrations were about 2200 and 500 cm^{-3} for the two MBL layers and the free troposphere layer, respectively. As discussed above, the MOUDI and denuder sampler data were used to construct the size-resolved chemical compositions of the layers, which are shown in Figure 5. Unlike other flights, the MOUDI sample taken in the free troposphere contained little Ca and Si, suggesting no significant mineral dust present. All three layers contained significant OC in the submicron size range, while only the layer at 600 m altitude contained significant EC.

The size distributions, together with the aerosol extinction distributions at 525 nm, were averaged for each layer (Figure 5). The aerosol extinction distributions are calculated at 525 nm since that wavelength is close to the peak solar irradiance wavelength and is one of those measured by AATS-14. All distributions shown correspond to aerosol at ambient conditions. Within the boundary layer, size

distributions at both altitudes are bimodal, with the major mode occurring at 70-80 nm, and the smaller mode at 20 nm. which may reflect result of recent nucleation events. The size distribution in the free troposphere layer was monomodal, with peak concentration at 140 nm. The aerosol extinction distributions indicate that submicron particles dominated total aerosol extinctions of all three layers at 525 nm.

The bottom panels in Figure 5 compare calculated aerosol extinctions using size distributions with those derived from the sunphotometer measurements, as well as showing vertical profiles of temperature, RH, and total particle concentration during the spiral. To facilitate comparison, the sunphotometer-derived aerosol extinction has been averaged to correspond to the DMA measurement interval. Comparison of vertical profiles of aerosol extinction at wavelengths 525 nm and 1059 nm are presented. As noted earlier, the uncertainty in aerosol extinction derived from AATS-14 measurement is ± 0.005 km^{-1}, which is introduced by the AOD smoothing procedure. [*Schmid et al.*, 2000]. The uncertainty, σ, in the predicted aerosol extinction based on the aerosol size distribution can be estimated by,

$$\sigma = \sqrt{\sum_i \sigma_i^2} \tag{10}$$

where σ_i is the uncertainty in predicted aerosol extinction associated with each individual uncertainty (Table 3). Except for the point near 600 m altitude (near the boundary of the free troposphere and marine boundary layer), the discrepancies between the aerosol extinctions lie within the estimated uncertainties. The disagreement near 600 m is likely a result of low vertical resolution of the DMA measurement. Aerosol

extinctions are also averaged over the boundary layer and the free troposphere, and the results are presented in Figure 5 as a function of wavelength. In both layers, the aerosol extinction calculated from the size distributions successfully reproduces the wavelength dependence from the AATS-14.

Figure 6.

Figure 6 shows the estimated uncertainties in the aerosol extinction calculation associated with each uncertainty category at 525 nm and 1059 nm. At both wavelengths and in both layers, the estimated uncertainty associated with the accuracy of aerosol size and concentration measurements dominates the overall uncertainty. Uncertainties introduced by assumptions concerning aerosol chemical composition are estimated to be generally within 10%. Estimated uncertainties for radiative closure calculated at 1059 nm are significantly larger than those at 525 nm. This is due to the uncertainties associated with APS measurement of supermicron particles, which contribute proportionately more to the total extinction at longer wavelength. The uncertainty due to the aerosol state, deliquesced vs. crystallized, is negligible for this profile, since in both layers the aerosol state can be accurately identified by comparing dry and "ambient" size distributions measured by the DMA system, that is, deliquesced at boundary layer and crystallized in free troposphere. The uncertainty arising from the method used to compute the particle refractive indices is negligible, and this will hold also in the other three cases.

Figure 7.

The derivation of aerosol extinction from AATS-14 data is based on the assumption that the path between the sun and the sunphotometer passes through horizontally homogeneous layers. The scattering coefficients measured by the onboard TSI 3-color nephelometer (model 3563) within each layer are used as an assessment of the layer

homogeneity. Figure 7 shows that the variation of scattering coefficients is small within each layer, suggesting that the assumption of horizontally homogeneous layers is supported for this flight, at least for layers sampled by the Twin Otter's horizontal legs. (As noted by *Russell et al.* [1999] and *Schmid et al.* [2000], horizontal and temporal variations of any attenuating layers above the aircraft can affect sunphotometer-derived extinction, but that does not appear to have occurred in this example.).

Figure 8.

3.2. Research Flight 12, April 19, 2001

Unlike the flight on April 23, a pollution layer with high aerosol extinction was observed between the boundary layer and free troposphere during Research Flight 12 along 133°E to 38°N on April 19, 2001 (Figure 8). The Twin Otter flew one-hour legs at 30 m (boundary layer) and 2000 m (pollution layer). The chemical composition of the pollution layer shows an enhanced contribution from nitrate, OC, and EC in the submicron size range, while the boundary layer is dominated by sulfate. The size distributions are monomodal except in the pollution layer. The size distribution of aerosol in the free tropospheric layer is similar to that of Research Flight 14, while in the boundary layer, the peak concentration size, 160 nm, is significantly larger than that of the previous case. Since neither MOUDI nor denuder filter samples were taken for the free tropospheric leg, the chemical composition from the previous flight on April 17 is used. Aerosol extinction during the spiral from UTC 2:37 to UTC 3:02 was calculated for the closure study. Agreement between observed and predicted aerosol extinction is not quite as close as for Research Flight 14. In the boundary layer, the

aerosol extinction calculated from the measured size distribution is larger than that derived from sunphotometer measurement at an altitude of 50 m, while smaller than that derived from sunphotometer measurement at 550 m. The discrepancies exceed the estimated uncertainties. While it is not possible to pinpoint the exact reason, the discrepancies in the boundary layer could result from the differentiation of AOD data, the vertical resolution of the DMA measurement, and horizontally inhomogeneous layers, as indicated by the variation in aerosol scattering coefficients (Figure 9). The oscillations of AATS-14 derived extinctions with respect to the predicted extinction is caused by spatial variability of the overlying AOD. Counting statistics of the size distribution measurements could account for the somewhat different extinction spectra in the free troposphere. To avoid over-smoothing of the AOD, the aerosol extinction is occasionally allowed to become negative, as seen in Figure 8. The observed and predicted aerosol extinctions are averaged over each layer, and in good agreement at 13 wavelengths measured by the AATS-14.

Figure 9.

Figure 10 shows the estimated uncertainties in the aerosol extinction calculation. Similar to Research Flight 14, the uncertainties associated with the accuracies of size and concentration measurements dominate the overall uncertainties in all calculations except in the free troposphere, where uncertainties introduced by the particle density become significant, especially at $\lambda = 1059$ nm. This is mainly a result of uncertainty in the mineral dust density, which is needed to interpret APS measurements for size distributions. Uncertainties due to the RH measurement and ram heating are negligible in both the pollution layer and free troposphere, because the ambient RH in each layer

Figure 10.

was very low, and the uncertainty in RH measurements does not encompass a change in size and calculated aerosol extinction of the crystallized aerosols.

3.3. Research Flight 11, April 17, 2001

Figure 11.

One focus of Research Flight 11 was to perform intercomparisons with R/V Ron Brown and the SeaWiFS satellite (Figure 11). The Twin Otter ferried to 33°N, 128°E, east of Cheju island. The Twin Otter performed one spiral at the time of the SeaWiFS overpass (UTC 5:52). A pollution layer was found between the boundary layer and the free troposphere. A backtrajectory calculation indicated that the pollution layer originated from mainland China. Unlike Research Flights 12 and 14, a dust layer was found in the free troposphere exhibiting significant aerosol extinction. MOUDI and denuder samples were taken at altitudes of 40, 1380, and 2810 m, and the resulting data were used to construct aerosol chemical composition in the boundary layer, pollution layer, and free troposphere. Total particle number concentrations in these three layers were about 5000, 2000, and 500 cm^{-3}, respectively. Aerosol number-vs-size distributions in all layers were monomodal to within the resolution of the linear y-axes shown in Figure 11. Compared to the boundary layer, the partice sizes at which the peak aerosol concentration were observed in the pollution layer and free troposphere were larger, suggesting more aged particles aloft. Aerosol extinction shows an increased contribution from supermicron particles to the total extinction at increasing altitude. In the pollution layer the extinction mode at diameter 2000 nm results from a surface area-vs-size mode not resolved in the $dN/dlogD_p$ plot.

Figure 12.

Radiative closure is addressed for the aircraft spiral at the time of SeaWiFS overpass at UTC 5:52. As shown in Figure 11, the size distribution-derived aerosol extinction is significantly smaller than that derived from the near-surface AATS-14 AOD measurement. Scattering coefficients measured during the flight are shown in Figure 12. Among all four cases that we consider here, the in-layer scattering coefficients displayed the most variability for this flight, especially within the pollution layer. The aerosol extinction calculated from the onboard measured size distribution is also supported by aerosol extinction derived from lidar measurement on R/V Ron Brown at the time of spiral (Figure 13), which shows a similar aerosol extinction and profile near the surface. Thus, the larger value of extinction obtained from AATS-14 is probably the result of temporal-horizontal variations of AOD on the photometer-to-sun path during the Twin Otter ascent from minimum altitude to 300 m.

Figure 13.

Figure 14.

For the pollution layer and free troposphere, the discrepancies between observed and calculated aerosol extinctions lie within the calculated uncertainties except for one point in the free troposphere (Figure 11). However, the aerosol extinctions calculated from measured size distributions are systematically smaller than those derived from AATS-14 measurements in the free troposphere. One possible cause is the error in the extrapolation of APS counting efficiency, which could significantly affect the aerosol extinction due to the large mineral dust particles.

That mineral dust particles are spherical is also physically unlikely. Without knowledge of the shape, dynamic shape factor, and ultra-Stokesian correction factor of the mineral dust, the aerosol extinction of nonspherical dust is estimated using the

data of doublet agglomerate particles from *Cheng et al.* [1993]. For doublet agglomerate particles consisting of two spheres, $\kappa = 1.142$, and the ultra-Stokesian correction factor is $1 + 0.1998\mathrm{Re}_\mathrm{p}^{0.6773}$. The aerosol extinction calculation of doublet agglomerates is based on the finding of *Mishchenko et al.* [1997] that the extinction of large nonspherical particles can be accurately predicted by that of spherical particles with the same surface-equivalent diameter. The calculated aerosol extinction is averaged over the mineral dust layer (Figure 14). By assuming a doublet agglomerate shape, the aerosol extinction calculated from the size distribution data is significantly larger than that assuming simply spherical particles. As a result, the calculated aerosol extinction is closer to, although somewhat larger than, that derived from the AATS-14. The increase is 49% at 525 nm and 60% at 1059 nm. The significant increase in aerosol extinction is due to two factors. First, for the same APS response, the volume-equivalent size derived by assuming a doublet agglomerate shape is larger than that derived assuming a spherical shape; second, for the same volume-equivalent size, nonspherical particles have a larger extinction cross-section because of larger surface-equivalent diameters. **Figure 15.**

The uncertainties in derived aerosol extinction are depicted in Figure 15. The uncertainties associated with the accuracy of the aerosol size and concentration measurements dominate the overall uncertainty expect in the mineral dust layer, where the uncertainty from particle density, mainly the mineral dust, becomes comparable. Note that Figure 15 excludes the uncertainties in dust particle shape discussed in the above paragraph. **Figure 16.**

3.4. Research Flight 9, April 14, 2001

The fourth of the cases studied focuses on the characterization of a mineral dust layer in free troposphere. The mineral dust layer during Research Flight 9 on April 14 exhibited the largest aerosol extinction among all cases studied. The Twin otter flight track, to 32.5°N, 132.5°E, south of Shikoku Island, the sampling of different layers, and the spiral for the radiative closure study are shown in Figure 16. APS data were not available during the sampling of the boundary layer and the beginning of the spiral; therefore, the analysis focuses on the pollution layer and the mineral dust layer in the free troposphere. Unlike previous cases, the total aerosol number concentration exhibits large variations within each layer. This could be a result of an ongoing mixing process of two different air masses, one of which is a polluted air mass with high particle number concentration. The mixing process is also evidenced by the RH profile during the spiral, which shows substantial vertical variation in the pollution layer. Aerosol extinction distributions are similar to those of Research Flight 11, on April 17, with a bimodal distribution in the pollution layer and a significant contribution of supermicron particles to the total aerosol extinction in the mineral dust layer.

Aerosol extinction closure is achieved again in the pollution layer on this flight. Similar to Research Flight 11 on April 17, aerosol extinctions calculated from the measured size distributions are systematically smaller than those derived from sunphotometer measurements. The discrepancy is probably a combined result of horizontally inhomogeneous aerosol layers during the spiral, which is shown by the large

variation of scattering coefficients during level flight in free troposphere (Figure 18), and inaccurate interpretation of APS data. The aerosol extinction is also calculated assuming a doublet agglomerate shape as described in the previous case, and the calculated aerosol extinction in the mineral dust layer is presented in Figure 17. The data suggest that the discrepancy could potentially be explained by the shape of the dust particles. The uncertainties in derived aerosol extinction are similar to those of Research Flight 11.

Figure 17.

Figure 18.

Figure 19.

3.5. Summary of Measured and Calculated Aerosol extinctions

Figure 19 shows measured and calculated aerosol extinctions over all four cases studied. (One data point near the surface during Research Flight 11 is excluded, where the aerosol extinction derived from AATS-14 measurement was probably corrupted as a result of horizontally inhomogeneous layers during the spiral.) The results show generally good agreement between aerosol extinction calculated from measured aerosol size distribution and chemical composition and those derived from sunphotometer measurements in boundary and pollution layers, where the slopes of the best fit are 0.96 and 1.03 at 525 nm and 0.94 and 1.04 at 1059 nm. For layers in the free troposphere, the slopes are 0.65 and 0.66 for 525 nm and 1059 nm, respectively. Possible reasons for underestimation of aerosol extinction from the size distribution data have been discussed above.

4. Summary

As part of the Aerosol Characterization Experiment-Asia from March to May 2001, aerosol size distributions were measured using differential mobility analyzer and aerodynamic particle sizer systems onboard the Twin Otter aircraft during 19 research flights. During the 19 missions, the atmosphere was often observed to be vertically layered, and a pollution layer with high aerosol extinction was frequently located between the boundary layer and free troposphere. Clear-column aerosol extinctions predicted using in situ aerosol size distribution and chemical composition measurements were compared to those derived from the 14-wavelength NASA Ames Airborne Tracking Sunphotometer (AATS-14). The uncertainties associated with predicted aerosol extinction are studied. In the boundary layer, pollution layers, and free troposphere with no significant mineral dust present, extinction closure was achieved within the estimated uncertainties over the full range of wavelengths of AATS-14. The aerosol extinctions predicted based on measured size distributions also reproduce the wavelength dependence derived from AATS-14 data. In free troposphere dust layers, the aerosol extinctions predicted from the measured size distributions were generally smaller than those derived from the AATS-14 data. The uncertainty analysis suggests that the discrepancy is likely a result of the lack of the knowledge of mineral dust shape, as well as variations in aerosol extinction derived from AATS-14 data when viewing through horizontally inhomogeneous layers. For all four research flights studied, the uncertainty in predicted aerosol extinction associated with the aerosol size and concentration

measurement accuracy dominates the overall uncertainty except in the dust layer, where the uncertainty introduced by lack of knowledge of dust density and shape becomes comparable. Considering all four cases, the best-fit lines yield Predicted/Observed ratios in boundary and pollution layers of 0.96 and 1.03 at $\lambda = 525$ nm, and 0.94 and 1.04 at $\lambda = 1059$ nm, respectively. For free tropospheric layers, the ratio is 0.65 and 0.66 at 525 nm and 1059 nm, respectively, when dust particles are modelled as spheres. A nonspherical model of dust (doublet agglomerates) can produce agreement between predicted and observed extinction, via the combined effect of larger APS-derived particle size and larger extinction-to-volume ratios.

Continued development of aerosol instruments, especially those capable of accurately characterizing the size and the shape of large particles, and size-resolved chemical composition will improve the ability to perform radiative closure of atmospheric aerosol.

5. Acknowledgement

We thank Brian Mader, Jose Jimenez, and Roya Bahreini for sharing their data. This work was supported by National Science Foundation Grant ATM-0001934, Office of Naval Research Grants N00014-96-1-0119 and N00014-01-F-0404, National Aeronautics and Space Administration Program Codes 622-44-75-10 and 291-01-91-45, and National Oceanographic and Atmospheric Administration Order NAO2AANRG0129.

References

Armendariz, A., and D. Leith, Concentration measurement and counting efficiency for the aerodynamic particle sizer 3320, *J. Aerosol Sci.*, *33*, 133–148, 2002.

Bahreini, R., J. Jimenez, F. R. C., J. Seinfeld, J. Jayne, and D. Worsnop, Aircraft-based Aerosol Size and Composition Measurements during ACE-Asia using an Aerodyne Aerosol Mass Spectrometer, *J. Geophys. Res.*, 2002.

Baron, P. A., *Aerosols*, (B. Y. H. Liu, D. Y. H. Pui, and H. J. Fissan, eds.), Elsevier, New York, 1984.

Bruggeman, D., Berechnung verschiedener physikalischer Konstanten von heterogenen Substanzen. I. Dielektrizitätskonstanten und Leitfähigkeiten der Mischkörper aus isotropen Substanzen, *Ann. Phys. (Leipzig)*, *24*, 636–679, 1935.

Cheng, Y., B. Chen, and H. Yeh, Behavior of isometric nonspherical aerosol- particles in the aerodynamic particle sizer, *J. Aerosol Sci.*, *21*, 701–710, 1990.

Cheng, Y., B. Chen, H. Yeh, I. Marshall, J. Mitchell, and W. Griffiths, Behavior of compact nonspherical particles in the TSI aerodynamic particle sizer model APS33B - Ultra-stokesian drag forces, *Aerosol Sci. Technol.*, *19*, 255–267, 1993.

Choi, J., M. Lee, Y. Chun, J. Kim, and S. Oh, Chemical composition and source signature of spring aerosol in Seoul, Korea, *J. Geophys. Res.*, *106*, 18,067–18,074, 2001.

Chylek, P., V. Srivastava, R. Pinnick, and R. Wang, Scattering of electromagnetic-

waves by composite spherical-particles - Experiment and effective medium approximations, *Appl. Opt.*, *27*, 2396–2404, 1988.

Clarke, A., J. Porter, F. Valero, and P. Pilewskie, Vertical profiles, aerosol microphysics, and optical closure during the Atlantic Stratocumulus Transition Experiment: Measured and modeled column optical properties, *J. Geophys. Res.*, *101*, 4443–4453, 1996.

Collins, D., R. C. Flagan, and J. H. Seinfeld, Improved inversion of scanning DMA data, *Aerosol Sci. Technol.*, *36*, 1–9, 2002a.

Collins, D., et al., In situ aerosol-size distributions and clear-column radiative closure during ACE-2, *Tellus*, *52B*, 498–525, 2000.

Collins, D., et al., Aerosol hygroscopic property closure during ACE-Asia, *J. Geophys. Res.*, 2002b.

CRC, *Handbook of Chemistry and Physics*, CRC Press, Cleveland, Ohio, 1970.

Fuller, K., W. Malm, and S. Kreidenweis, Effects of mixing on extinction by carbonaceous particles, *J. Geophys. Res.*, *104*, 15,941–15,954, 1999.

Gao, S., et al., Airborne measurements of chemical species during ACE-Asia: Their identification and spatial distribution., *J. Geophys. Res.*, 2002.

Griffiths, W., P. Iles, and N. Vaughan, The behavior of liquid droplet aerosols in an APS- 3300, *J. Aerosol Sci.*, *17*, 921–930, 1986.

He, K., F. Yang, Y. Ma, Q. Zhang, X. Yao, C. Chan, S. Cadle, T. Chan, and P. Mulawa,

The characteristics of PM2.5 in Beijing, China, *Atmos. Environ.*, *35*, 4959–4970, 2001.

Hegg, D., J. Livingston, P. Hobbs, T. Novakov, and P. Russell, Chemical apportionment of aerosol column optical depth off the mid-Atlantic coast of the United States, *J. Geophys. Res.*, *102*, 25,293–25,303, 1997.

Hoff, R., L. GuiseBagley, R. Staebler, H. Wiebe, J. Brook, B. Georgi, and T. Dusterdiek, Lidar, nephelometer, and in situ aerosol experiments in southern Ontario, *J. Geophys. Res.*, *101*, 19,199–19,209, 1996.

Howell, S., and B. Huebert, Determining marine aerosol scattering characteristics at ambient humidity from size-resolved chemical composition, *J. Geophys. Res.*, *103*, 1391–1404, 1998.

Huebert B., et al., The Aerosol Characterization Experiment-Asia (ACE-Asia), *J. Geophys. Res.*, 2002.

Kim, Y., J. Lee, N. Baik, J. Kim, S. Shim, and C. Kang, Summertime characteristics of aerosol composition at Cheju Island, Korea, *Atmos. Environ.*, *32*, 3905–3915, 1998.

Kinney, P., and D. Pui, Inlet efficiency study for the TSI aerodynamic particle sizer, *Particle & Particle Systems Characterization*, *12*, 188–193, 1995.

Larson, S., G. Cass, K. Hussey, and F. Luce, Verification of image-processing based visibility models, *Environ. Sci. Technol.*, *22*, 629–637, 1988.

Mader, B., R. C. Flagan, and J. H. Seinfeld, Aircraft measurements of atmospheric carbonaceous aerosols during ACE-Asia, *J. Geophys. Res.*, Submitted, 2002.

Moelwyn-Hughes, E. A., *Physical Chemistry*, Pergamon, New York, 1961.

Nenes, A., S. Pandis, and C. Pilinis, ISORROPIA: A new thermodynamic equilibrium model for multiphase multicomponent inorganic aerosols, *Aquat. Geochem.*, *4*, 123–152, 1998.

Redemann, J., R. Turco, R. Pueschel, M. Fenn, E. Browell, and W. Grant, A multi-instrument approach for characterizing the vertical structure of aerosol properties: Case studies in the Pacific Basin troposphere, *J. Geophys. Res.*, *103*, 23,287–23,298, 1998.

Russell, P., J. Livingston, P. Hignett, S. Kinne, J. Wong, A. Chien, R. Bergstrom, P. Durkee, and P. Hobbs, Aerosol-induced radiative flux changes off the United States mid-Atlantic coast: Comparison of values calculated from sunphotometer and in situ data with those measured by airborne pyranometer, *J. Geophys. Res.*, *104*, 2289–2307, 1999.

Saxena, P., L. Hildemann, P. McMurry, and J. Seinfeld, Organics alter hygroscopic behavior of atmospheric particles, *J. Geophys. Res.*, *100*, 18,755–18,770, 1995.

Schmid, B., et al., Clear-sky closure studies of lower tropospheric aerosol and water vapor during ACE-2 using airborne sunphotometer, airborne in-situ, space-borne, and ground-based measurements, *Tellus*, *52B*, 568–593, 2000.

Schmid, B., et al., Coordinated airborne, spaceborne, and ground-based measurements

of massive, thick aerosol layers during the dry season in Southern Africa, *J. Geophys. Res.*, *Submitted*, 2002.

Sokolik, I., A. Andronova, and T. Johnson, Complex refractive-index of atmospheric dust aerosols, *Atmos. Environ.*, *27A*, 2495–2502, 1993.

Tang, I., Chemical and size effects of hygroscopic aerosols on light scattering coefficients, *J. Geophys. Res.*, *101*, 19,245–19,250, 1996.

Tang, I., and H. Munkelwitz, Water activities, densities, and refractive-indexes of aqueous sulfates and sodium-nitrate droplets of atmospheric importance, *J. Geophys. Res.*, *99*, 18,801–18,808, 1994.

Tang, I., A. Tridico, and K. Fung, Thermodynamic and optical properties of sea salt aerosols, *J. Geophys. Res.*, *102*, 23,269–23,275, 1997.

Turpin, B., and H. Lim, Species contributions to PM2.5 mass concentrations: Revisiting common assumptions for estimating organic mass, *Aerosol Sci. Technol.*, *35*, 602–610, 2001.

Videen, G., and P. Chylek, Scattering by a composite sphere with an absorbing inclusion and effective medium approximations, *Opt. Commun*, *158*, 1–6, 1998.

Volz, F., Infrared optical constants of ammonium sulfate, sahara dust, volcanic pumice and flyash, *Appl. Opt.*, *12*, 564–568, 1973.

Wang, H., and W. John, Particle density correction for the aerodynamic particle sizer, *Aerosol Sci. Technol.*, *6*, 191–198, 1987.

Wang, J., R. Flagan, and J. Seinfeld, A differential mobility analyzer (DMA) system for submicron aerosol measurements at ambient relative humidity, *Aerosol Sci. Technol.*, In press, 2002.

Wilson, J., and B. Liu, Aerodynamic particle-size measurement by laser- doppler velocimetry, *J. Aersol Sci.*, *11*, 139–150, 1980.

John H. Seinfeld, California Institute of Technology, 1200 E. California Blvd., Pasadena, California

Received _____

Figure Captions

Figure 1. APS correlated data, taken during Research Flight 9 on April 14, 2001. Two data masks used to remove artificial particles are indicated by the solid and dashed lines. The x-axis is the light scattering channel, which increases with increasing intensity of light scattered by particles. The y-axis is the time of flight channel, which increases with increasing particle time of flight between two detection laser beams, and is an indication of particle size.

Figure 2. Schematic diagram of the inlet system for airborne APS measurement.

Figure 3. APS counting efficiency from *Armendariz and Leith* [2001] and $\eta_{\mathrm{asp}}\eta_{\mathrm{tran}}$ for APS model 3310 from *Kinney and Pui* [1995].

Figure 4. Ambient size distributions derived from DMA and APS measurements in a layer at 450 m altitude during Research Flight 17 on April 27, 2001 .

Figure 5. Size distributions, chemical compositions, and aerosol extinction comparison for Research Flight 14 on April 23, 2001. The panels are: flight track, total particle number concentration and flight altitude. Ambient size distributions, aerosol extinction size distributions averaged over the indicated layers (BL=Boundary layer, PL=Pollution layer, and FT=Free troposphere), size resolved chemical compositions. RH, temperature, and total number concentration profiles during the spiral. Comparison of observed and predicted vertical profiles of aerosol extinction at 525 and 1059 nm. The comparison of aerosol extinction is averaged over each layer as a function of wavelength. Uncertainty limits of derived and observed aerosol extinction are blue and red, respectively.

Figure 6. Estimated uncertainties in the aerosol extinction calculation based on measured size distribution and chemical composition for Research Flight 14 on April 23, 2001.

Figure 7. Scattering coefficients measured by onboard TSI 3-color nephelometer (model 3563) during Research Flight 14 on April 23, 2001. The wavelengths are 450 nm, 550 nm, and 700 nm.

Figure 8. Same format as Figure 5. Data and aerosol extinction comparison of Research Flight 12 on April 19, 2001.

Figure 9. Scattering coefficients measured by onboard TSI 3-color nephelometer (model 3563) during Research Flight 12 on April 19, 2001. The wavelengths are 450 nm, 550 nm, and 700 nm.

Figure 10. Estimated uncertainties in the aerosol extinction calculation based on measured size distribution and chemical composition for Research Flight 12 on April 19, 2001.

Figure 11. Same format as Figure 5. Data and aerosol extinction comparison of Research Flight 11 on April 17, 2001.

Figure 12. Scattering coefficients measured by onboard TSI 3-color nephelometer (model 3563) during Research Flight 11 on April 17, 2001. The wavelengths are 450 nm, 550 nm, and 700 nm.

Figure 13. Comparison of aerosol extinction derived from AATS-14 measurement, aerosol size distributions, and Lidar measurements on R/V Ron Brown during the spiral of Research flight 11 on April 17, 2001.

Figure 14. Aerosol extinctions averaged over the dust layer of Research Flight 11 on April 17, 2001. The calculation of aerosol extinction is based on a doublet agglomerate particle shape. The dashed and solid lines are the estimated uncertainties in measured and predicted extinctions, respectively.

Figure 15. Estimated uncertainties in the aerosol extinction calculation based on measured size distribution and chemical composition for Research Flight 11 on April 17, 2001.

Figure 16. Same format as Figure 5. Data and aerosol extinction comparison of Research Flight 9 on April 14, 2001.

Figure 17. Aerosol extinctions averaged over the dust layer of Research Flight 9 on April 14, 2001. The calculation of aerosol extinction is based on a doublet agglomerate particle shape. The dashed and solid lines are the estimated uncertainties in measured and predicted extinctions, respectively.

Figure 18. Scattering coefficients measured by onboard TSI 3-color nephelometer (model 3563) during Research Flight 9 on April 14, 2001. The wavelengths are 450 nm, 550 nm, and 700 nm.

Figure 19. Comparison of measured and predicted aerosol extinctions and best-fit lines of calculation/measurement. The data are from the four flights analyzed.

Tables

Table 1. Measurements made on board the Twin Otter that are related to this study.

Property measured	**Size range**	**Instrument**	**Time resolution**
Aerosol microphysics			
Aerosol size distribution	0.015-1μm	Differential mobility analyzer system	100 s
Aerosol size distribution	0.5-20μm	Aerodynamic particle sizer	20 s
Aerosol hygroscopicity	0.040-0.6μm	Tandem DMA system	20 min
Aerosol composition			
Inorganic anions, elements	$< 3\mu$m	MOUDI sampler	30 min - 1 h
OC, EC	$< 2.3\mu$m	Denuder sampler	30 min - 1 h
Optical property			
Aerosol optical depth		14-wavelength sunphotometer	4 s
Aerosol scattering coefficient		TSI 3563 nephelometer	1 s
Meteorological measurement			
Pressure, temperature, and RH		Various	1s

Table 2. The concentration of NH_4^+, SO_4^{2-}, and NO_3^- during recent studies of aerosol chemical composition in East Asia. Unit: $\mu g/m^3$

Reference	NH_4^+	SO_4^{2-}	NO_3^-	Molar ratio $NH_4^+/(2SO_4^{2-}+NO_3^-)$	Location
He et al. (2001)	4.28	10.15	7.26	0.72	Beijing, China
Choi et al. (2001)	4.5	7.28	8.04	0.89	Seoul, South Korea
Choi et al. (2001)	5.51	12.79	13.14	0.64	Seoul, South Korea
Choi et al. (2001)	3.87	11.16	8.16	0.59	Seoul, South Korea
Kim et al. (1998)	2.81	8.4	0.89	0.82	Cheju, South Korea

Table 3. Assumed levels of uncertainty associated with properties required for calculation of aerosol extinction from aerosol size distribution and composition measurements.

Uncertainty source	**Base value**	**Uncertainty**
Deliquescence and efflorescence		
Deliquesced?	N/A	N/A
Mixing state		
Mixing state	Internal	External
RH measurements and ram heating		
Ambient RH	N/A	±1%
RH inside DMA	N/A	±3%
APS ram heating	1.2°C	1°C,2°C
Accuracy of size and conc. measurement		
DMA size	N/A	±5%
DMA concentration	N/A	±10%
APS size	N/A	±10%
APS concentration	N/A	±20% ($< 5\mu$m),±50% ($\geq 5\mu$m)
APS data mask	Custom	TSI carbon
Chemical composition		
$NH_4^+/(2{\cdot}SO_4^{2-}+NO_3^-)$	0.75	±0.25
m_{oc}/m_c	2.1	±0.2
m_{ions}/m_{carbon}	N/A	±30%
m_{dust}/m_{coarse}	N/A	±0.2
D_{p0} in Eqn. 5	N/A	×1.5,/1.5
α in Eqn. 5	3.3	2.7,4.3
Particle density		
Dust density	2.5	±30%
OC density	1.2	±20%
EC density	2.0	1.9,2.1
Effective refractive index		
Eff. refractive index	Bruggeman	Volume average

Figures

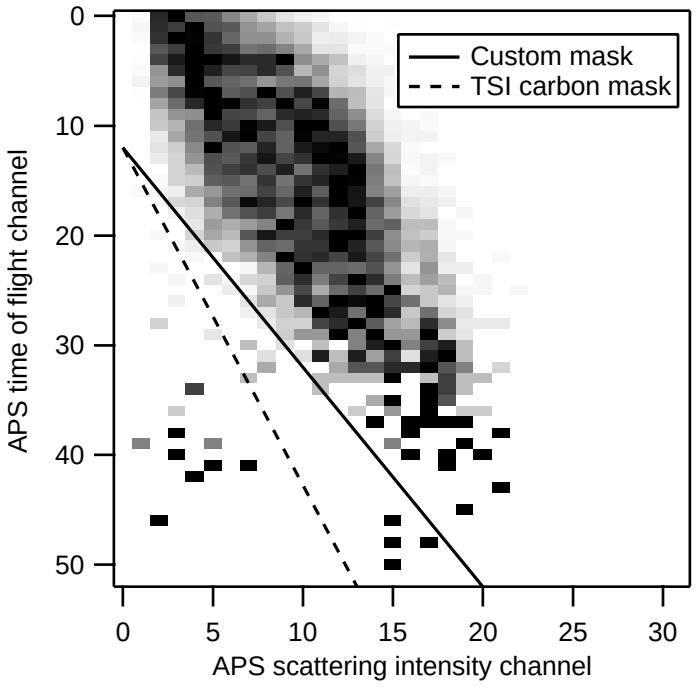

Figure 1. APS correlated data, taken during Research Flight 9 on April 14, 2001. Two data masks used to remove artificial particles are indicated by the solid and dashed lines. The x-axis is the light scattering channel, which increases with increasing intensity of light scattered by particles. The y-axis is the time of flight channel, which increases with increasing particle time of flight between two detection laser beams, and is an indication of particle size.

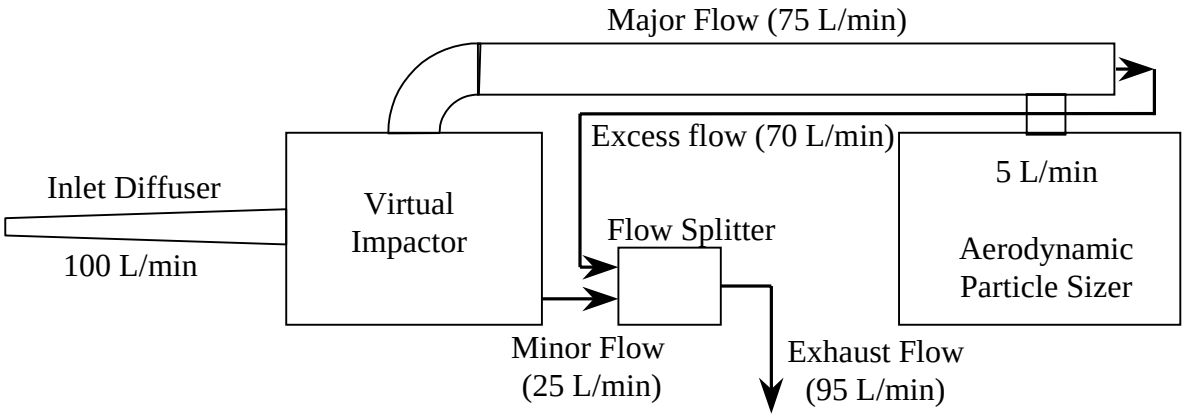

Figure 2. Schematic diagram of the inlet system for airborne APS measurement.

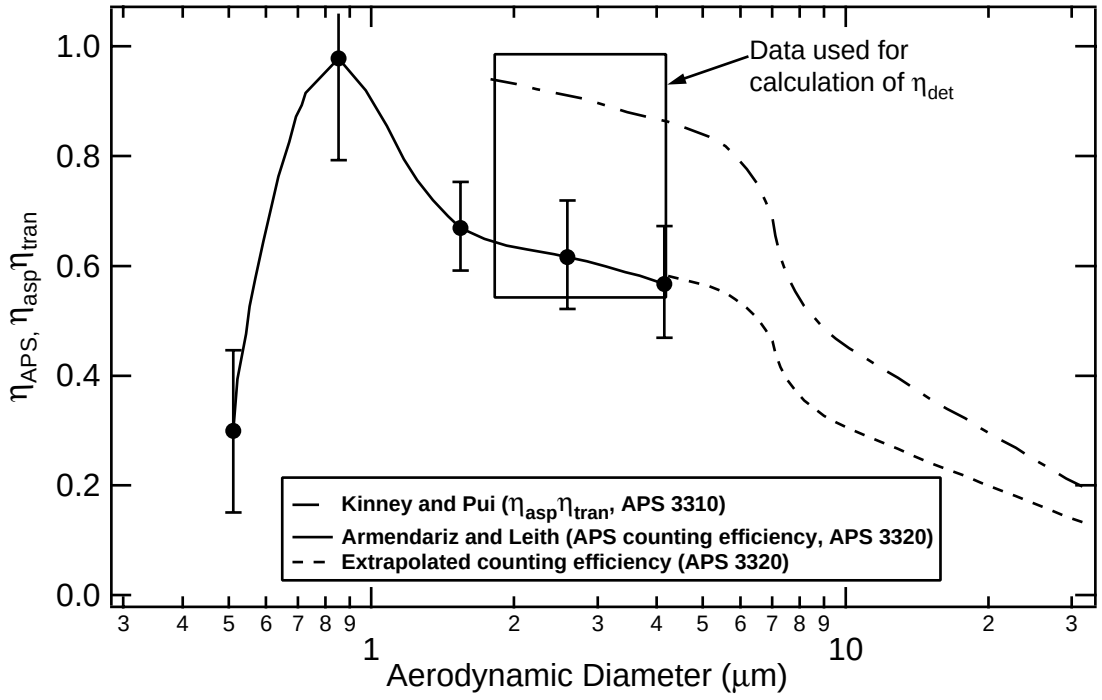

Figure 3. APS counting efficiency from *Armendariz and Leith* [2001] and $\eta_{\rm asp}\eta_{\rm tran}$ for APS model 3310 from *Kinney and Pui* [1995].

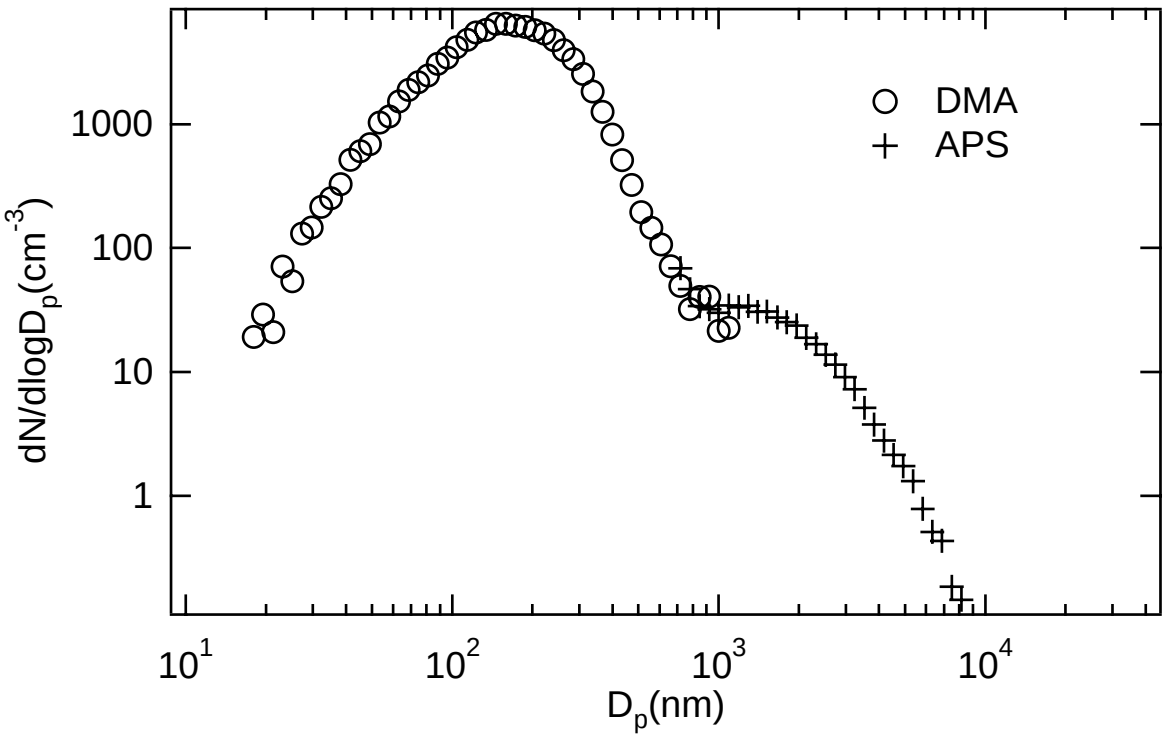

Figure 4. Ambient size distributions derived from DMA and APS measurements in a layer at 450 m altitude during Research Flight 17 on April 27, 2001 .

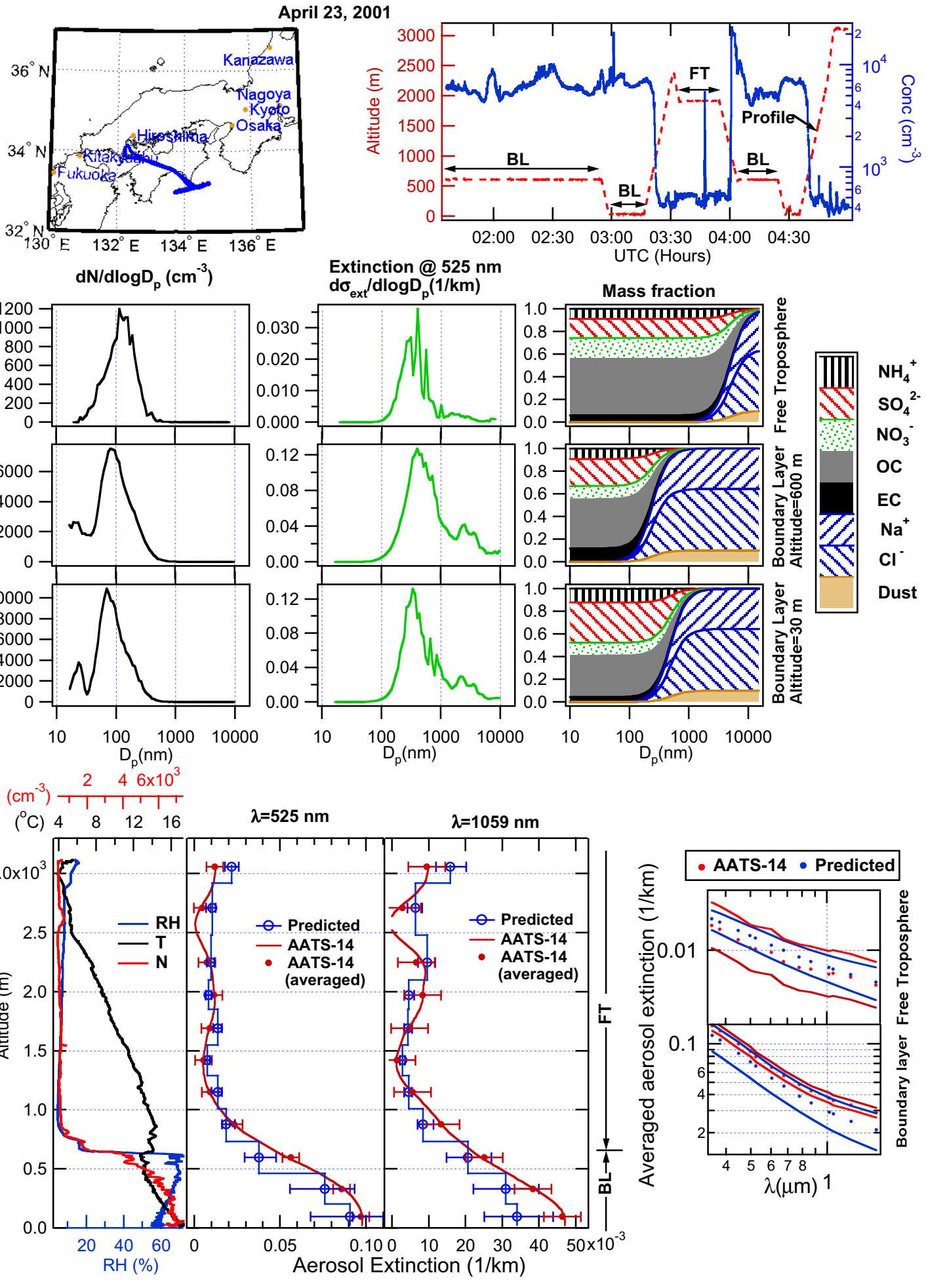
April 23, 2001
Kanazawa
Nagoya
Kyoto
Osaka
Hiroshima
Kitakyushu
Fukuoka
36° N
34° N
32° N
130° E
132° E
134° E
136° E
Altitude (m)
Conc (cm-3)
FT
Profile
BL
BL
BL
02:00
02:30
03:00
03:30
04:00
04:30
UTC (Hours)
dN/dlogDp (cm-3)
Extinction @ 525 nm
dσext/dlogDp(1/km)
Mass fraction
Free Troposphere
Boundary Layer Altitude=600 m
Boundary Layer Altitude=30 m
NH4+
SO4 2-
NO3-
OC
EC
Na+
Cl-
Dust
Dp(nm)
(cm-3)
(°C)
λ=525 nm
λ=1059 nm
RH
T
N
Predicted
AATS-14
AATS-14 (averaged)
RH (%)
Aerosol Extinction (1/km)
FT
BL
AATS-14
Predicted
Averaged aerosol extinction (1/km)
λ(μm)
Free Troposphere
Boundary layer

Paste flight 14, April 23, 2001 graph here

Figure 5. Size distributions, chemical compositions, and aerosol extinction comparison for Research Flight 14 on April 23, 2001. The panels are: flight track, total particle number concentration and flight altitude. Ambient size distributions, aerosol extinction size distributions averaged over the indicated layers (BL=Boundary layer, PL=Pollution layer, and FT=Free troposphere), size resolved chemical compositions. RH, temperature, and total number concentration profiles during the spiral. Comparison of observed and predicted vertical profiles of aerosol extinction at 525 and 1059 nm. The comparison of aerosol extinction is averaged over each layer as a function of wavelength. Uncertainty limits of derived and observed aerosol extinction are blue and red, respectively.

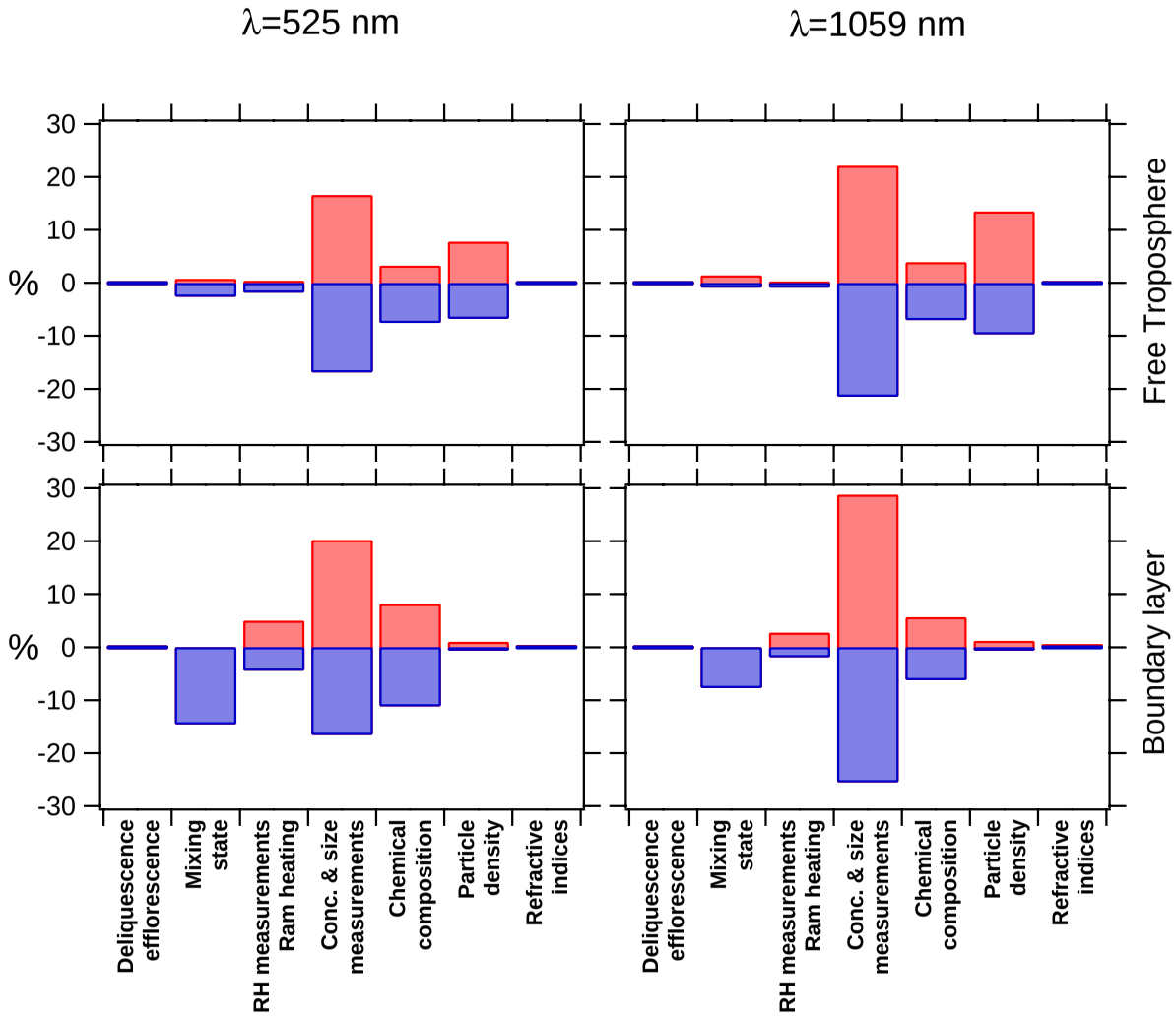

Figure 6. Estimated uncertainties in the aerosol extinction calculation based on measured size distribution and chemical composition for Research Flight 14 on April 23, 2001.

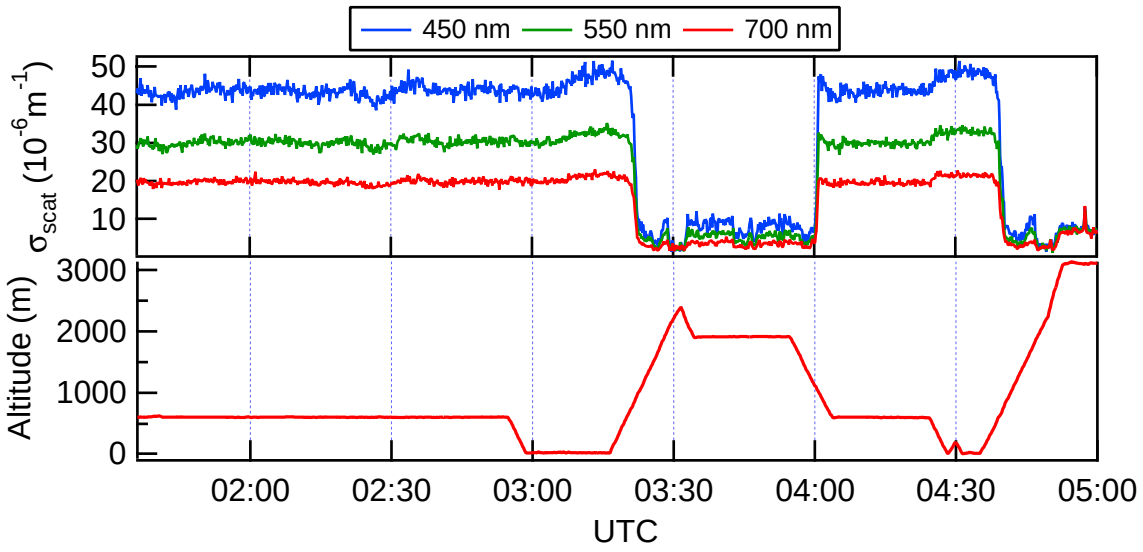

Figure 7. Scattering coefficients measured by onboard TSI 3-color nephelometer (model 3563) during Research Flight 14 on April 23, 2001. The wavelengths are 450 nm, 550 nm, and 700 nm.

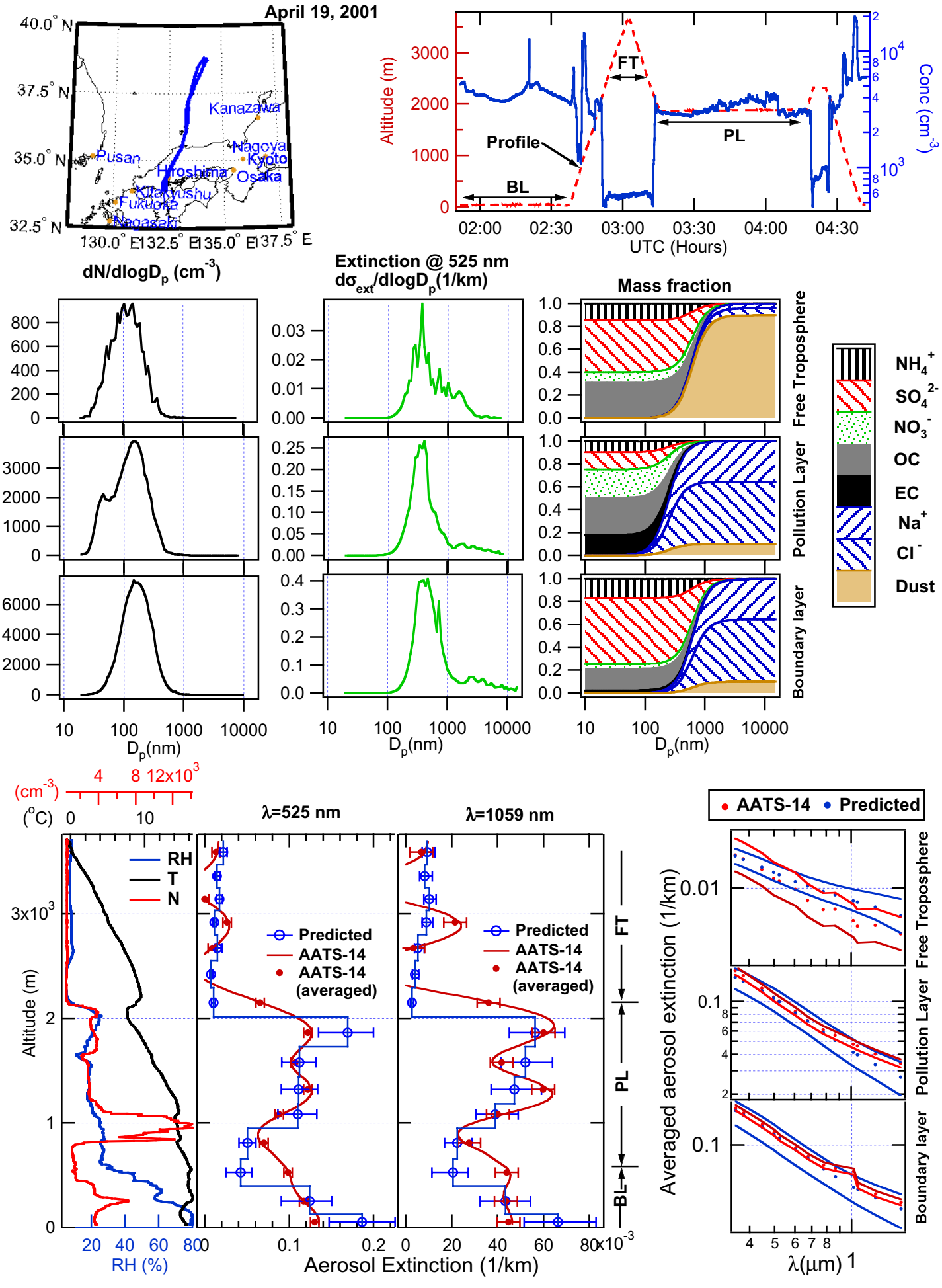
April 19, 2001
40.0° N
37.5° N
35.0° N
32.5° N
130.0° E
132.5° E
135.0° E
137.5° E
Kanazawa
Nagoya
Kyoto
Osaka
Pusan
Hiroshima
Kitakyushu
Fukuoka
Nagasaki
Altitude (m)
Conc (cm-3)
FT
PL
BL
Profile
UTC (Hours)
dN/dlogDp (cm-3)
Extinction @ 525 nm
dσext/dlogDp(1/km)
Mass fraction
Free Troposphere
Pollution Layer
Boundary layer
NH4+
SO42-
NO3-
OC
EC
Na+
Cl-
Dust
Dp(nm)
(cm-3)
(°C)
RH
T
N
λ=525 nm
λ=1059 nm
Predicted
AATS-14
AATS-14 (averaged)
RH (%)
Aerosol Extinction (1/km)
AATS-14
Predicted
Averaged aerosol extinction (1/km)
λ(μm)

Paste flight on April 19, 2001 graph here

Figure 8. Same format as Figure 5. Data and aerosol extinction comparison of Research Flight 12 on April 19, 2001.

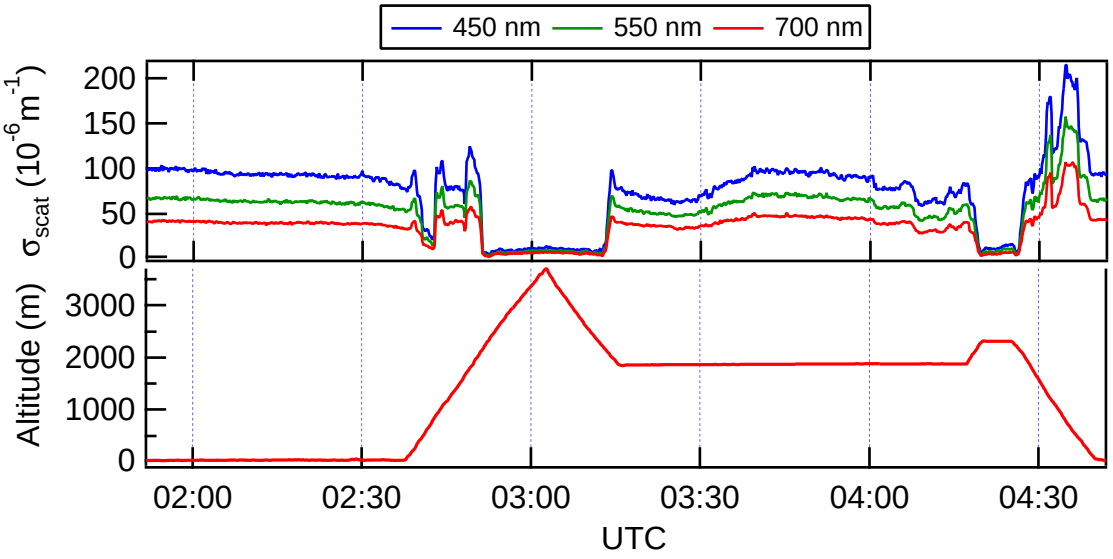

Figure 9. Scattering coefficients measured by onboard TSI 3-color nephelometer (model 3563) during Research Flight 12 on April 19, 2001. The wavelengths are 450 nm, 550 nm, and 700 nm.

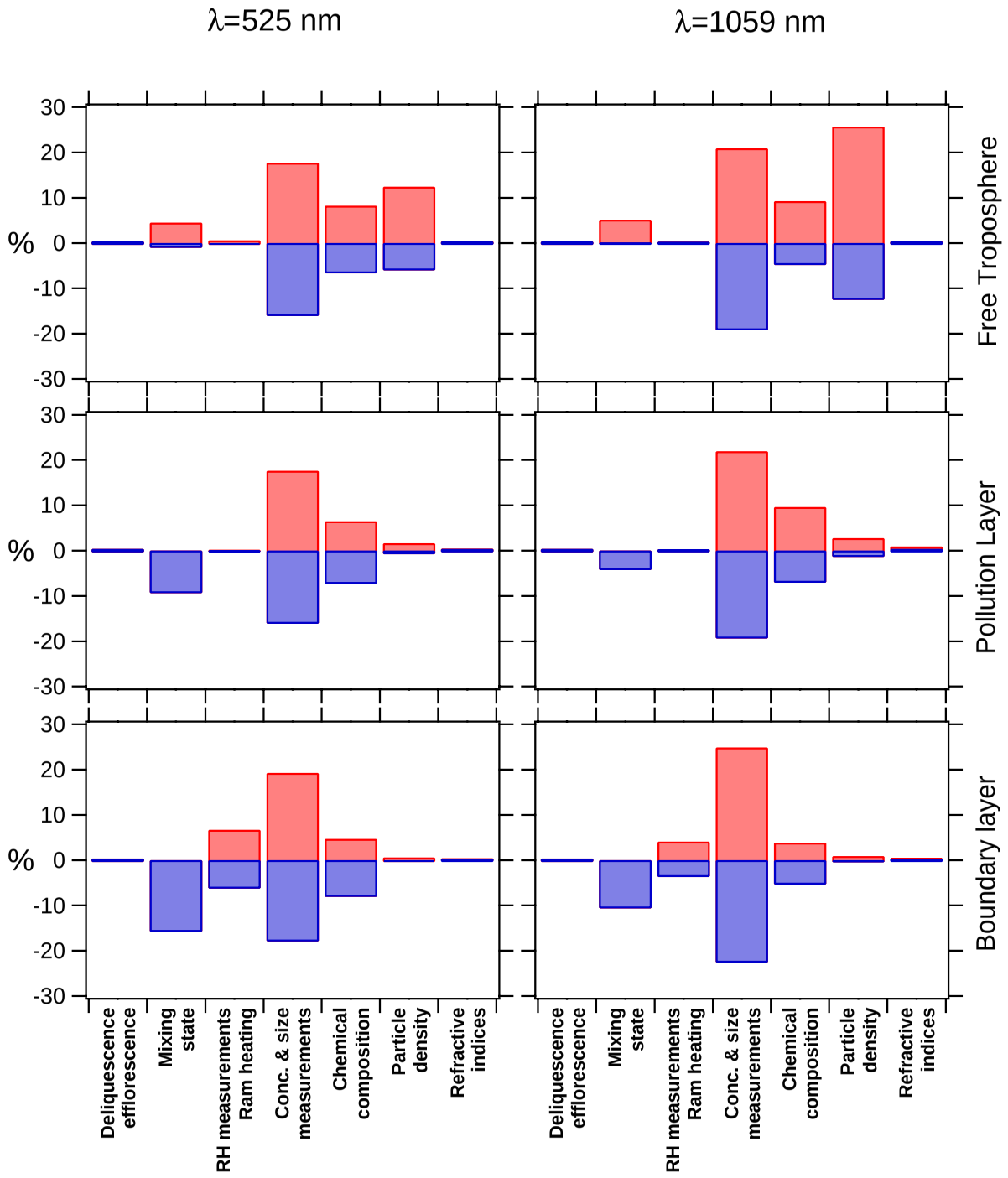

Figure 10. Estimated uncertainties in the aerosol extinction calculation based on measured size distribution and chemical composition for Research Flight 12 on April 19, 2001.

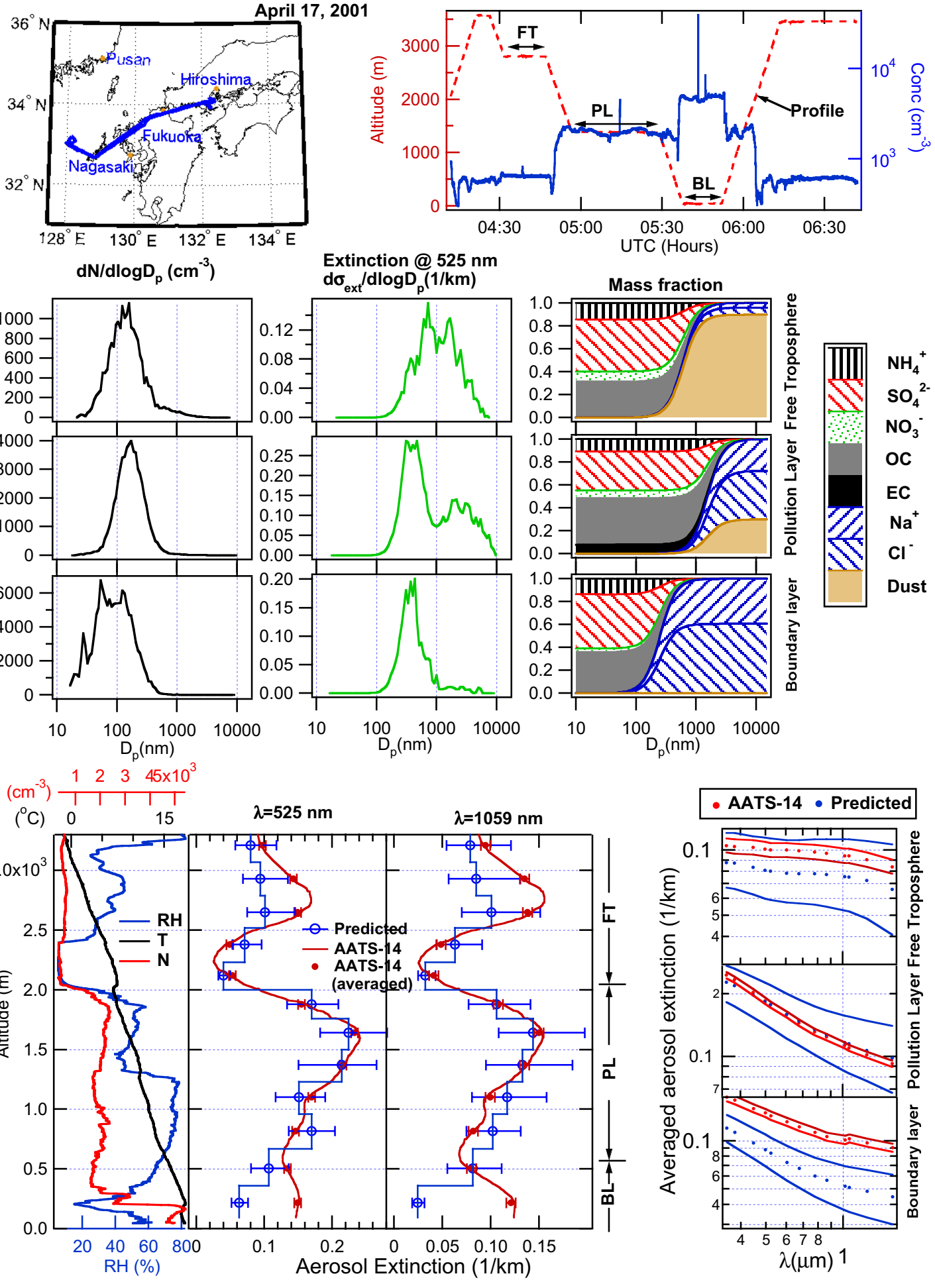
April 17, 2001
36° N
34° N
32° N
128° E
130° E
132° E
134° E
Pusan
Hiroshima
Fukuoka
Nagasaki
FT
PL
BL
Profile
Altitude (m)
Conc (cm-3)
UTC (Hours)
04:30
05:00
05:30
06:00
06:30
dN/dlogDp (cm-3)
Extinction @ 525 nm
dσext/dlogDp(1/km)
Mass fraction
Free Troposphere
Pollution Layer
Boundary layer
NH4+
SO42-
NO3-
OC
EC
Na+
Cl-
Dust
Dp(nm)
(cm-3)
(°C)
λ=525 nm
λ=1059 nm
RH
T
N
Predicted
AATS-14
AATS-14 (averaged)
RH (%)
Aerosol Extinction (1/km)
AATS-14
Predicted
Averaged aerosol extinction (1/km)
λ(μm)

Paste flight 11, April 17, 2001 graph here

Figure 11. Same format as Figure 5. Data and aerosol extinction comparison of Research Flight 11 on April 17, 2001.

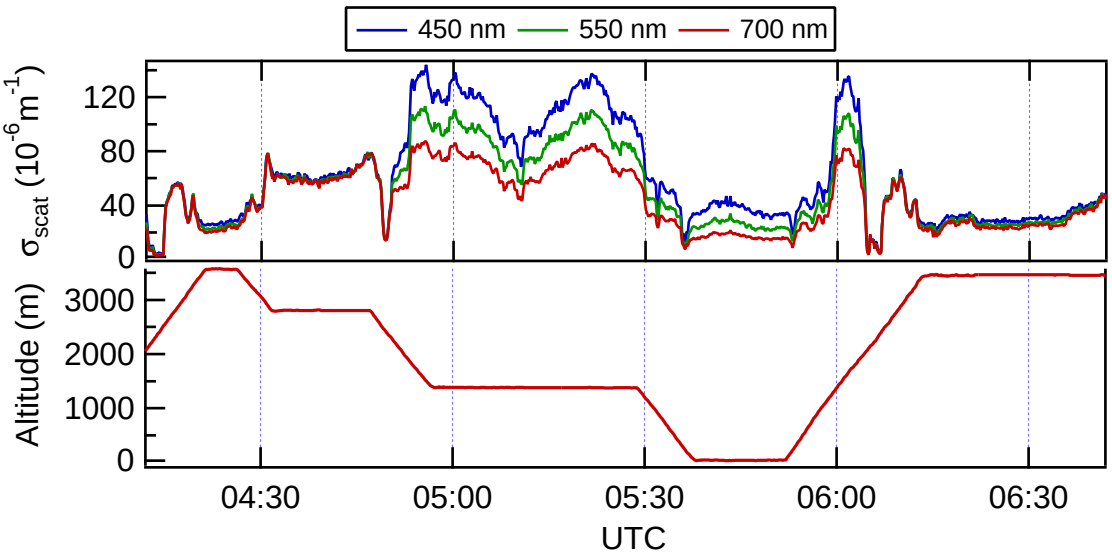

Figure 12. Scattering coefficients measured by onboard TSI 3-color nephelometer (model 3563) during Research Flight 11 on April 17, 2001. The wavelengths are 450 nm, 550 nm, and 700 nm.

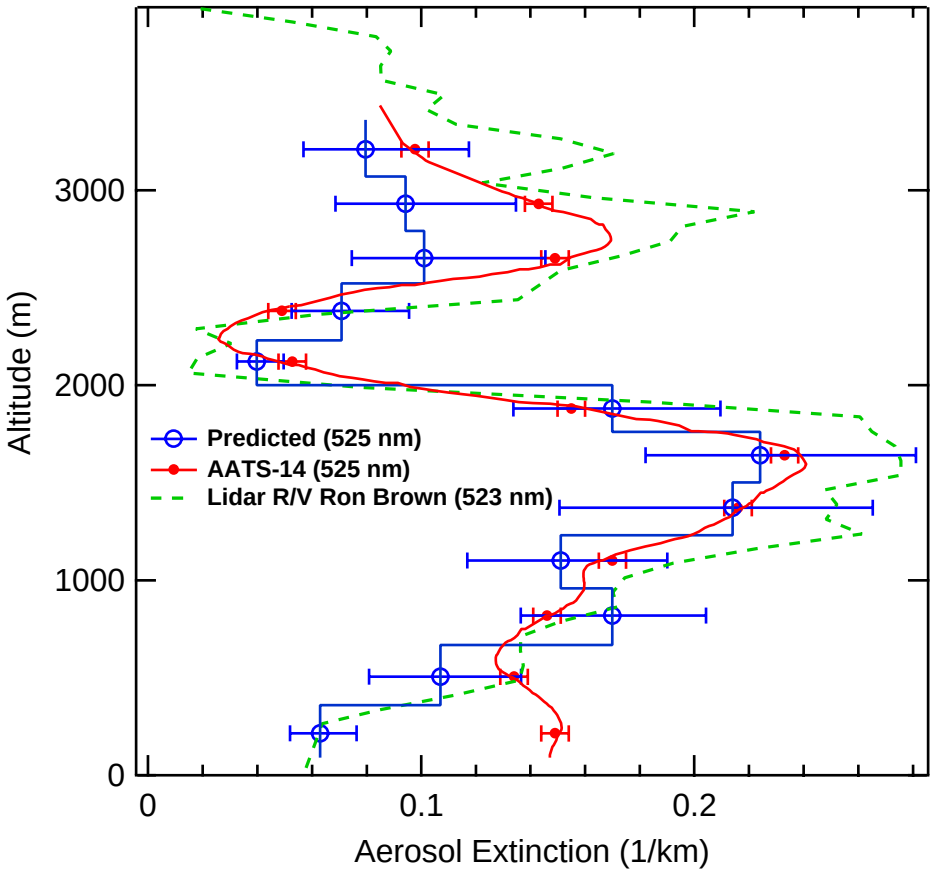

Figure 13. Comparison of aerosol extinction derived from AATS-14 measurement, aerosol size distributions, and Lidar measurements on R/V Ron Brown during the spiral of Research flight 11 on April 17, 2001.

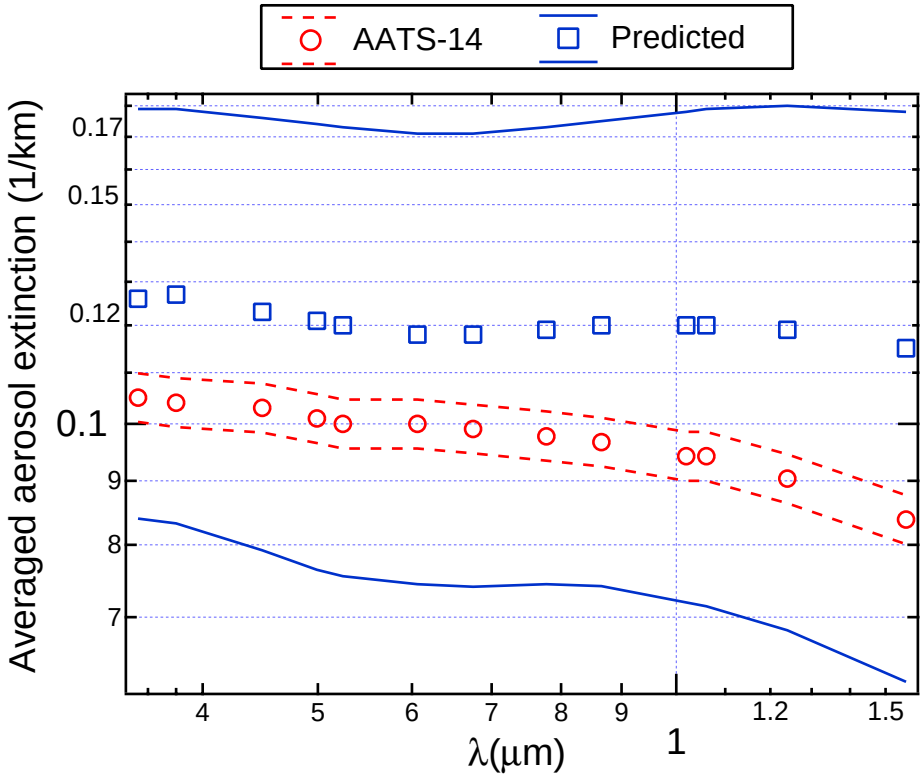

Figure 14. Aerosol extinctions averaged over the dust layer of Research Flight 11 on April 17, 2001. The calculation of aerosol extinction is based on a doublet agglomerate particle shape. The dashed and solid lines are the estimated uncertainties in measured and predicted extinctions, respectively.

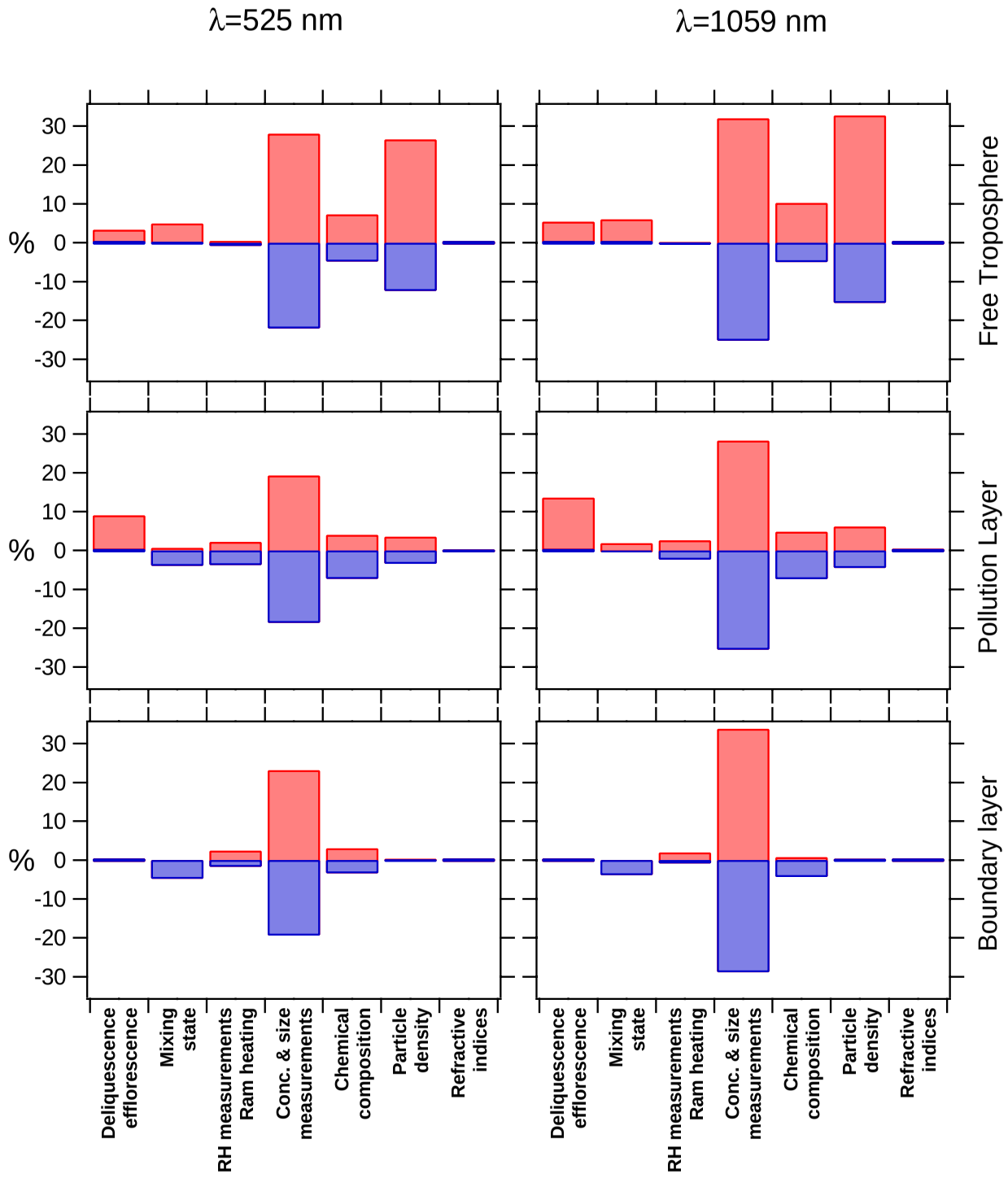

Figure 15. Estimated uncertainties in the aerosol extinction calculation based on measured size distribution and chemical composition for Research Flight 11 on April 17, 2001.

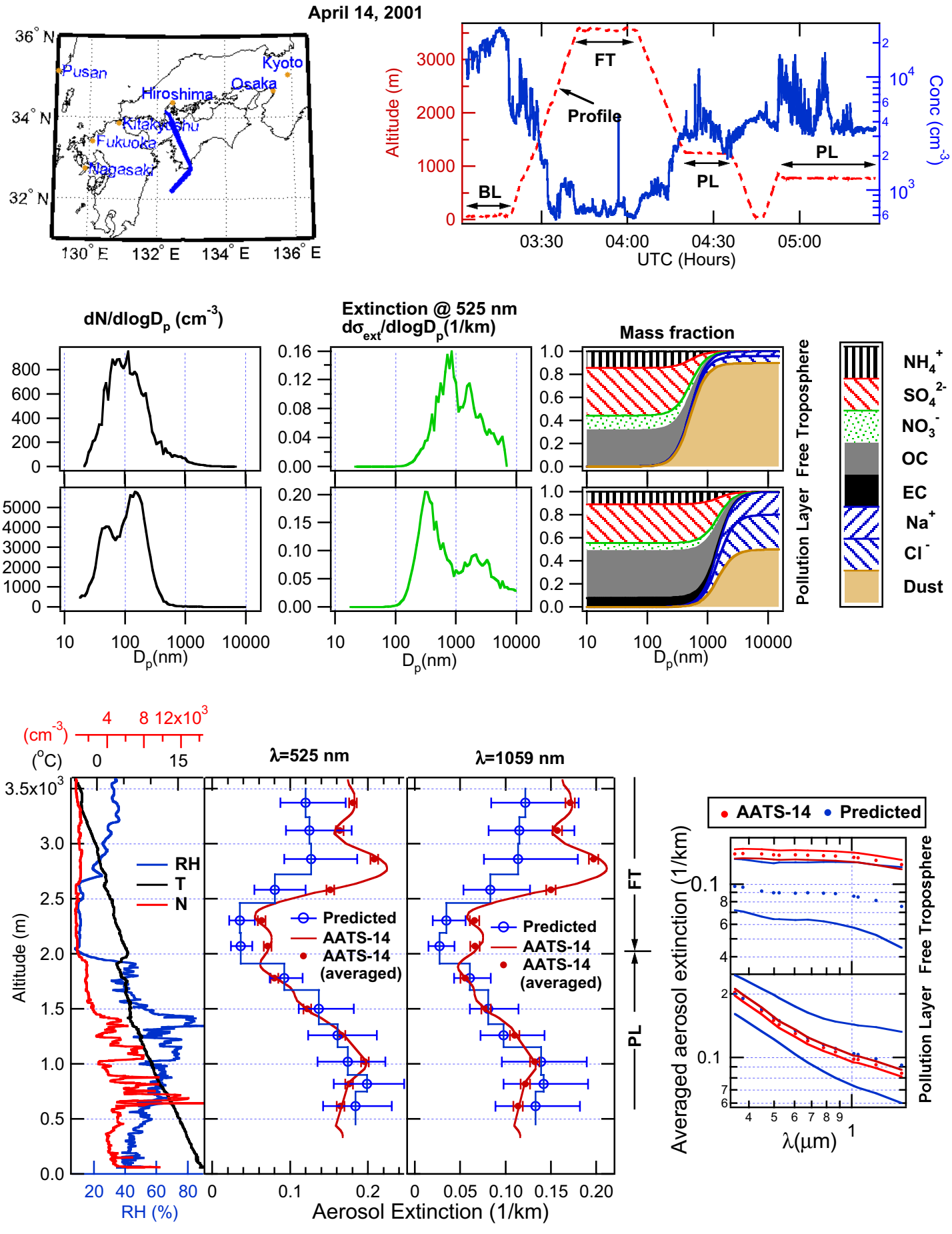
April 14, 2001
36° N
34° N
32° N
130° E
132° E
134° E
136° E
Pusan
Kyoto
Osaka
Hiroshima
Kitakyushu
Fukuoka
Nagasaki
Altitude (m)
3000
2000
1000
0
FT
Profile
BL
PL
PL
Conc (cm-3)
03:30
04:00
04:30
05:00
UTC (Hours)
dN/dlogDp (cm-3)
Extinction @ 525 nm
dσext/dlogDp(1/km)
Mass fraction
Free Troposphere
Pollution Layer
NH4+
SO4 2-
NO3-
OC
EC
Na+
Cl-
Dust
Dp(nm)
(cm-3)
4
8
12x10^3
(°C)
0
15
λ=525 nm
λ=1059 nm
RH
T
N
Predicted
AATS-14
AATS-14 (averaged)
RH (%)
Aerosol Extinction (1/km)
FT
PL
AATS-14
Predicted
Averaged aerosol extinction (1/km)
λ(μm)
Free Troposphere
Pollution Layer

Paste flight on April 14, 2001 graph here

Figure 16. Same format as Figure 5. Data and aerosol extinction comparison of Research Flight 9 on April 14, 2001.

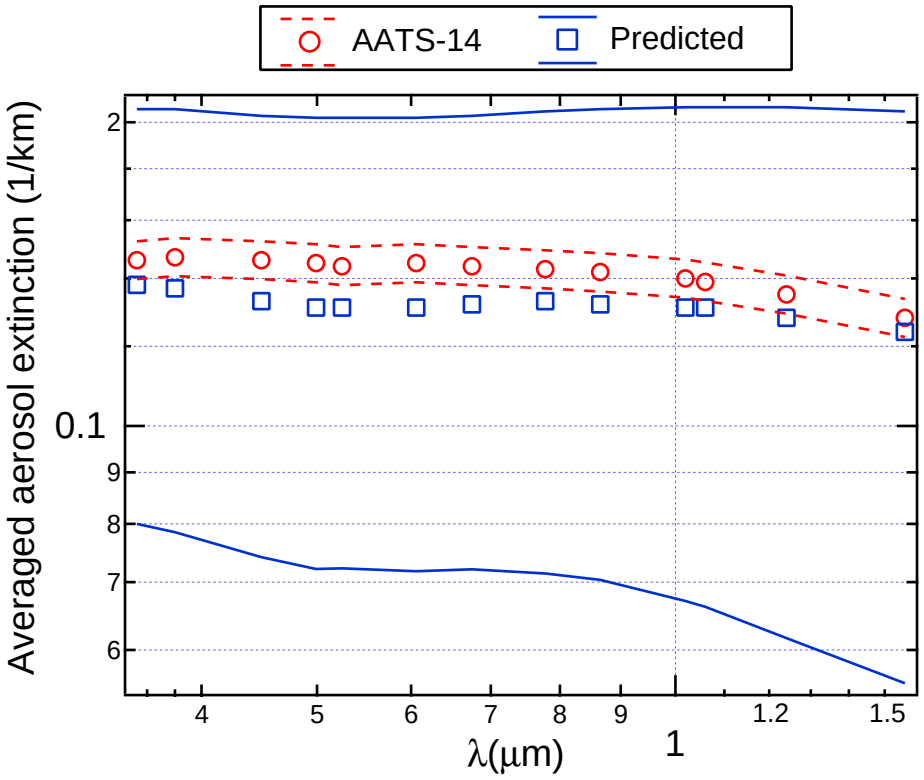

Figure 17. Aerosol extinctions averaged over the dust layer of Research Flight 9 on April 14, 2001. The calculation of aerosol extinction is based on a doublet agglomerate particle shape. The dashed and solid lines are the estimated uncertainties in measured and predicted extinctions, respectively.

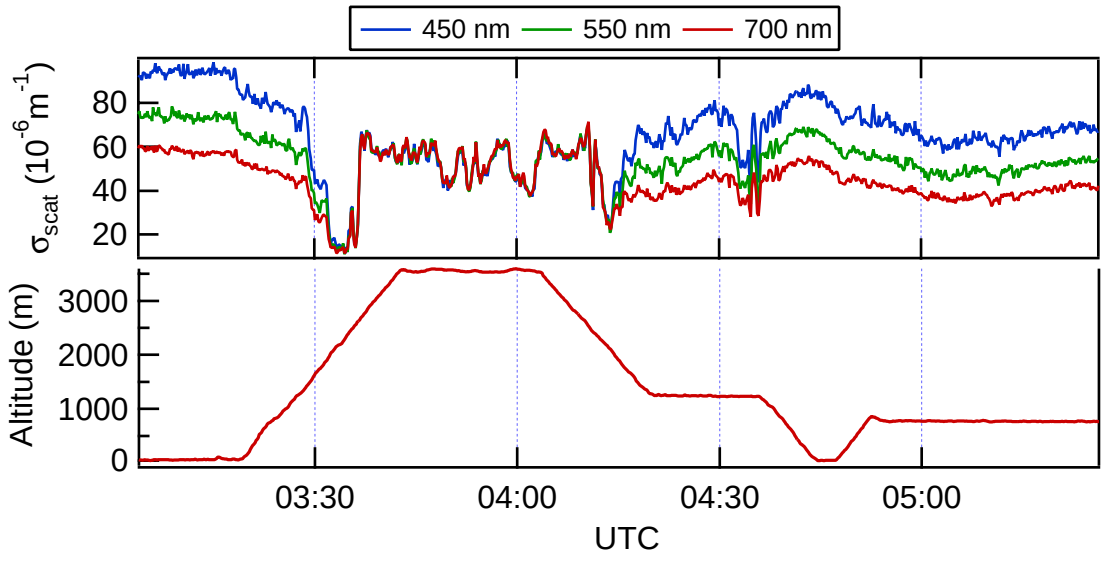

Figure 18. Scattering coefficients measured by onboard TSI 3-color nephelometer (model 3563) during Research Flight 9 on April 14, 2001. The wavelengths are 450 nm, 550 nm, and 700 nm.

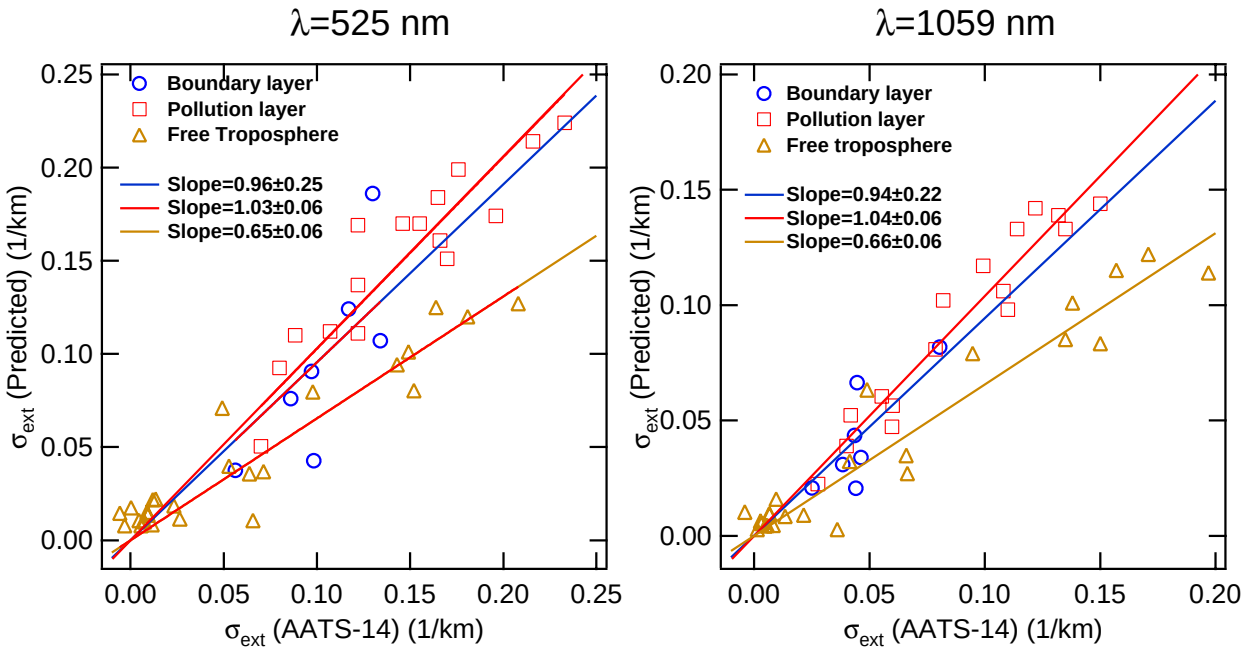

Figure 19. Comparison of measured and predicted aerosol extinctions and best-fit lines of calculation/measurement. The data are from the four flights analyzed.